ผลของสัณฐานวิทยาของ TiO_2 ต่อประสิทธิภาพของเซลล์สุริยะชนิดเพอรอฟสไกต์
$CH_3NH_3PbI_3$

นางสาวรมณ ทรงธนสิทธิ์

วิทยานิพนธ์นี้เป็นส่วนหนึ่งของการศึกษาตามหลักสูตรปริญญาวิทยาศาสตรมหาบัณฑิต
สาขาวิชาฟิสิกส์ ภาควิชาฟิสิกส์
คณะวิทยาศาสตร์ จุฬาลงกรณ์มหาวิทยาลัย
ปีการศึกษา 2560
ลิขสิทธิ์ของจุฬาลงกรณ์มหาวิทยาลัย

EFFECT OF TiO$_2$ MORPHOLOGY ON EFFICIENCY OF CH$_3$NH$_3$PbI$_3$

PEROVSKITE SOLAR CELLS

Miss Ramon Songtanasit

จุฬาลงกรณ์มหาวิทยาลัย

CHULALONGKORN UNIVERSITY

A Thesis Submitted in Partial Fulfillment of the Requirements
for the Degree of Master of Science Program in Physics
Department of Physics
Faculty of Science
Chulalongkorn University
Academic Year 2017

Thesis Title	EFFECT OF TiO$_2$ MORPHOLOGY ON EFFICIENCY OF CH$_3$NH$_3$PbI$_3$ PEROVSKITE SOLAR CELLS
By	Miss Ramon Songtanasit
Field of Study	Physics
Thesis Advisor	Assistant Professor Sojiphong Chatraphorn, Ph.D.
Thesis Co-Advisor	Thiti Taychatanapat, Ph.D.

Accepted by the Faculty of Science, Chulalongkorn University in Partial Fulfillment of the Requirements for the Master's Degree

.... Dean of the Faculty of Science
(ProfessorPolkit Sangvanich, Ph.D.)

THESIS COMMITTEE

.... Chairman
(Assistant Professor Rattachat Mongkolnavin, Ph.D.)

.... Thesis Advisor
(Assistant Professor Sojiphong Chatraphorn, Ph.D.)

.... Thesis Co-Advisor
(Thiti Taychatanapat, Ph.D.)

.... Examiner
(Orapin Wannadelok, Ph.D.)

.... External Examiner
(Assistant ProfessorRachsak Sakdanuphab, Ph.D.)

รมณ ทรงธนสิทธิ์ : ผลของสัณฐานวิทยาของ TiO_2 ต่อประสิทธิภาพของเซลล์สุริยะชนิด
เพอรอฟสไกต์ $CH_3NH_3PbI_3$ (EFFECT OF TiO_2 MORPHOLOGY ON
EFFICIENCY OF $CH_3NH_3PbI_3$ PEROVSKITE SOLAR CELLS) อ.ที่ปรึกษา
วิทยานิพนธ์หลัก: ผศ. ดร.โศจิพงศ์ ฉัตราภรณ์, อ.ที่ปรึกษาวิทยานิพนธ์ร่วม: ดร.ธิติ เตช
ธนพัฒน์, 61 หน้า.

ชั้นคอมแพ็ค (cp) หรือชั้นบล็อกกิ้งของไทเทเนียมไดออกไซด์ (TiO_2) มีความสำคัญใน
เซลล์สุริยะชนิดเพอรอฟสไกต์ซึ่งผสมระหว่างสารอินทรีย์ อนินทรีย์ ตะกั่วกับเฮไลด์ เนื่องจากชั้น
ไทเทเนียมไดออกไซด์ ป้องกันการรวมตัวกันของคู่พาหะบริเวณรอยต่อระหว่างชั้นดีบุกออกไซด์
โด๊บด้วยฟลูออรีน (FTO) กับ ชั้นเพอรอฟสไกต์ได้ ในงานวิจัยนี้จะทำการสังเคราะห์ วิเคราะห์ชั้น
cp-TiO_2 และศึกษาผลของชั้น cp-TiO_2 ที่มีต่อเซลล์สุริยะชนิดเพอรอฟสไกต์ ในงานวิจัยนี้ชั้น cp-
TiO_2 ถูกสังเคราะห์โดยวิธีอาร์เอฟแมกเนตรอนสปัตเตอริงกับวิธีหมุนเคลือบโดยเปลี่ยนสภาวะ
ต่างๆ ชั้น cp-TiO_2 จะถูกรวมอยู่ในโครงสร้างของเซลล์สุริยะชนิดเพอรอฟสไกต์ซึ่งประกอบด้วย
Au/spiro-OMeTAD/MAPbI3/mp-TiO_2/cp-TiO_2/FTO สำหรับวิธีการสปัตเตอริง cp-
TiO_2 สามารถบล็อกการส่งผ่านของโฮลจากชั้นไทเทเนียมไดออกไซด์ ไปยังชั้น FTO แต่อาจไม่
เหมาะสมในการถ่ายโอนอิเล็กตรอนจากชั้นเพอรอฟสไกต์ไปยังชั้น FTO ส่วนวิธีหมุนเคลือบ
พบว่าชั้น cp-TiO_2 ที่สังเคราะห์ได้ไม่สามารถบล็อกการส่งผ่านของโฮลจากชั้นไทเทเนียมได
ออกไซด์ไปยังชั้น FTO ได้ทั้งหมด แต่กลับสามารถนำไปใช้เป็นชั้นส่งผ่านอิเล็กตรอนในเซลล์
สุริยะชนิดเพอรอฟสไกต์ได้ ค่าความกว้างของช่องว่างระหว่างแถบพลังงานของไทเทเนียมได
ออกไซด์ ที่สังเคราะห์โดยวิธีสปัตเตอริงและวิธีหมุนเคลือบอยู่ในช่วง 3.65 – 3.77 eV ซึ่ง
สอดคล้องกับเฟสอนาเทส อย่างไรก็ตามลักษณะทางสัณฐานวิทยาของไทเทเนียมไดออกไซด์ ที่
สังเคราะห์โดยทั้งสองวิธี ไม่เหมือนกัน สำหรับวิธีสปัตเตอริงลักษณะทางสัณฐานวิทยาของชั้นไท
เทเนียมไดออกไซด์เหมือนกันกับชั้น FTO แต่สำหรับวิธีหมุนเคลือบ เกรนของไทเทเนียมได
ออกไซด์บน FTO มีลักษณะเป็นเม็ดเล็กๆค่อนข้างกลม ซึ่งสังเกตได้จาก AFM phase images ซึ่ง
ส่งผลโดยตรงต่อประสิทธิภาพของเซลล์สุริยะชนิดเพอรอฟสไกต์ พบว่าสภาวะที่ให้ประสิทธิภาพดี
ที่สุดคือสปินชั้นคอมแพคและชั้นมีรูพรุนขนาดมีโซของไทเทเนียมไดออกไซด์ที่ 5000 รอบต่อ
นาที เป็นเวลา 30 วินาที ซึ่งให้ประสิทธิภาพสูงสุดประมาณ 6.55%

ภาควิชา	ฟิสิกส์	ลายมือชื่อนิสิต	_____
สาขาวิชา	ฟิสิกส์	ลายมือชื่อ อ.ที่ปรึกษาหลัก	_____
ปีการศึกษา	2560	ลายมือชื่อ อ.ที่ปรึกษาร่วม	_____

5772113123 : MAJOR PHYSICS

KEYWORDS: PEROVSKITE SOLAR CELL / TITANIUM DIOXIDE / SPUTTERING

RAMON SONGTANASIT: EFFECT OF TiO_2 MORPHOLOGY ON EFFICIENCY OF $CH_3NH_3PbI_3$ PEROVSKITE SOLAR CELLS. ADVISOR: ASST. PROF. SOJIPHONG CHATRAPHORN, Ph.D., CO-ADVISOR: THITI TAYCHATANAPAT, Ph.D., 61 pp.

A TiO_2 compact (cp) layer or blocking layer (bl) plays a crucial role in a hybrid organic-inorganic lead halide perovskite solar cell (PSC) because it prevents the carrier recombination at the interface of fluorine-doped tin oxide (FTO) and perovskite layers. In this work, fabrication, characterizations of cp-TiO_2 and their effects on the PSC were studied. The cp-TiO_2 layers in this work were fabricated by radio frequency (RF)-magnetron sputtering method and spin coating method with various conditions. The cp-TiO_2 layer was incorporated into the PSC device structure consisting of Au/spiro-OMeTAD/MAPbI$_3$/mp-TiO_2/cp-TiO_2/FTO. For the sputtering method, cp-TiO_2 could selectively block the transport of holes from TiO_2 to the FTO layer, but it might not be appropriate to transfer electrons from the perovskite layer to the FTO. For a spin coating method, TiO_2 layer cannot completely block the transport of holes from TiO_2 to the FTO layer, but it can be used as an electron transporting layer for PSCs. Energy gaps of TiO_2 by sputtering and spin coating were found to be in the range of 3.65 – 3.77 eV corresponding to the anatase phase. However, morphologies of TiO_2 fabricated by sputtering and spin coating methods are not the same. For the sputtering method, morphology of TiO_2 layer is similar to FTO. For spin coating, there are very fine round grains of TiO_2 on FTO surface as observed in the AFM phase images. This directly affects the performance of the PSCs. It is found that the best condition for spin coating of compact and mesoporous TiO_2 layers is 5,000 rpm for 30 s with the corresponding maximum power conversion efficiency of about 6.6%.

Department:	Physics	Student's Signature	
Field of Study:	Physics	Advisor's Signature	
Academic Year:	2017	Co-Advisor's Signature	

ACKNOWLEDGEMENTS

CONTENTS

LIST OF TABLES

LIST OF FIGURES

CHAPTER I
INTRODUCTION

1.1 Overview

Nowadays, people around the world use a lot of energy per day for their activities in everyday life. Increasing energy demand and awareness about global warming lead to the concern about alternative sources of energy. One of the most interesting alternative sources of renewable energy is solar energy because energy from the sun falls on the earth in one hour more than it is used by everyone in the world in one year. There are several recent technologies for converting solar energy into electricity such as organic photovoltaic cells (OPVs) [1], dye sensitized solar cells (DSSCs) [2] and quantum dot solar cells (QDSCs) [3, 4]. Additionally, hybrid organometal halide perovskites, derived from DSSCs as light absorbers, get more attention due to the unprecedentedly rapid improvement of perovskite solar cells its power conversion efficiency [5].

Perovskite is a type of materials that have the same structure as calcium titanium oxide ($CaTiO_3$). Perovskite structure is in a form of ABX_3. It consists of BX_6 octahedra that locates at the corners of a cubic with A at the center. A and B are cations of different sizes and X is an anion. For the hybrid organic-inorganic halide perovskite, A is an organic cation usually methylammonium ($CH_3NH_3^+$), ethylammonium ($CH_3CH_2NH_3^{3+}$), or formamidinium ($NH_2CH=NH_2^+$), B is a metal cation usually Sn^{2+} or Pb^{2+} and X is an anion or a halogen usually Cl^-, Br^-, I^-, or mixed halide material [6].
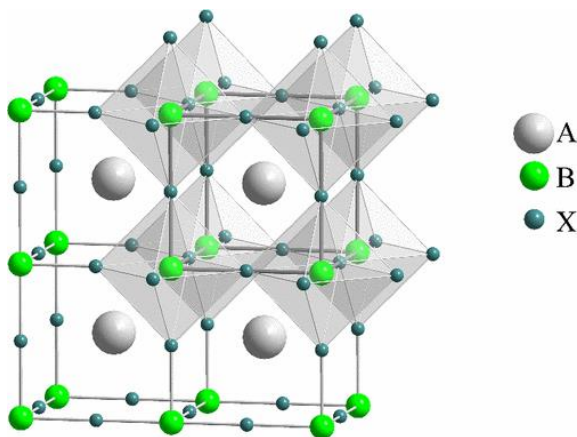
Figure 1 Schematic diagram represents ABX_3 perovskite crystal structure [7].

In 1991, DSSCs were first fabricated by O'Regan and Grätzel [8]. A DSSC consists of a transparent conducting oxide electrode such as fluorine-doped tin oxide (FTO) or indium-doped tin oxide (ITO), a dye-sensitized mesoporous semiconductor metal oxide film such as nanocrystalline TiO_2, counter electrode such as a platinum (Pt), and an electrolyte containing redox couples such as I^-/I^{3-} dissolved in a solvent. This device architecture has power conversion efficiencies (PCEs) up to 13% [9]. However, there are some problems with this device such as potential leakage problems from corrosive and volatile nature of the liquid electrolyte. This problem was solved in 1998 by using a solid hole-transporting material (HTM) 2,2′,7,7′-tetrakis (N,N-di-p-methoxyphenylamine)-9,9′-spirobifluorene (spiro-OMeTAD or, in short as, spiro) instead of the conventional liquid redox electrolyte [10]. These devices are called solid-state dye-sensitized solar cells (ss-DSSCs). In 2012, Grätzel *et al.* [11] and Snaith *et al.* [12] used $CH_3NH_3PbI_3$ ($MAPbI_3$) and $CH_3NH_3PbI_2Cl$ ($MAPbI_2Cl$) perovskite nanocrystals for absorber layer and submicron thick mesoporous TiO_2 film and spiro-OMeTAD for an electron- and a hole-transporting layer, respectively. Initially, the PCEs were 9.7% and 7.6% and there had long term stability [12]. Additionally, Snaith *et al.* also used insulating mesoporous Al_2O_3 instead of mesoporous TiO_2. The FTO/blocking layer (bl)-TiO_2/mesoporous (mp)-Al_2O_3/$MAPbI_2Cl$/spiro-OMeTAD/Ag-based device showed a PCE of 10.9% [12]. Etgar *et al.* fabricated solar cells with FTO/bl-TiO_2/mp-TiO_2/$MAPbI_3$/Au and achieved a PCE of 5.5% [13]. All of the aforementioned studies showed that there were many types of perovskite solar cells (PSCs) depending on materials that were used. Moreover, most types of PSC need bl-TiO_2 or compact (cp)-TiO_2.

Cp-TiO_2 blocking layers are indispensable and play critical roles in preventing the carrier recombination at the interface of FTO and perovskite layer and avoiding short-circuit. So, high quality TiO_2 blocking layers are necessary to achive high PCE. There are several methods to fabricate cp-TiO_2 layer such as aerosol spray pyrolysis [14-16], thermal oxidation [17], spin-coating method [18], atomic layer deposition [19], and electrochemical deposition [20]. Gao *et al.*[21] compared deposition methods of cp-TiO_2 between magnetron sputtering (MS) and sol-gel (SG). They employed a TiO_2 for target to sputter TiO_2 blocking layer. It was found that TiO_2 from sputtering method is more compact and can give high efficiency devices (Figure 2(E)). Therefore, the

different morphological properties between MS-TiO$_2$ and SG-TiO$_2$ blocking layers that shown in Figure 2(a) - (d) can affect the performance of these solar cells.

Chen *et al.* [22] fabricated TiO$_2$ by radio frequency (RF)-magnetron sputtering using TiO$_2$ target with a purity 99.99% and 52 mm in diameter. The sputtering processes were sputtered in pure Ar gas at a working pressure 3.5 Pa. and used sputtering power of 120 W. They studied the influence of TiO$_2$ layer on PSCs with varying sputtering time. The results are shown in Figure 3. When the sputtering time is increased from 15 to 30 min as increasing cp-layer thickness, the J$_{sc}$ increased. It means
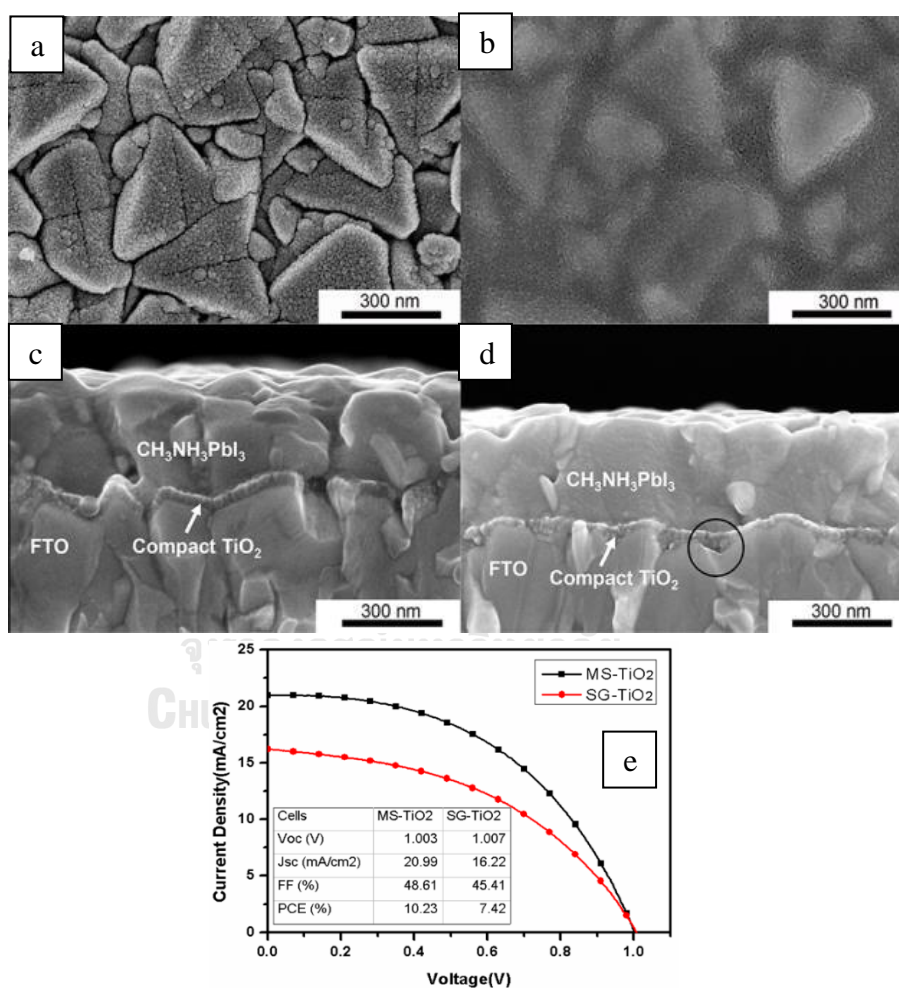
Figure 2 (a, b) Top-view and (c, d) cross-section FE-SEM images of TiO$_2$ blocking layers prepared by magnetron sputtering (MS-TiO$_2$) and solgel (SG-TiO$_2$) methods, respectively (The black circle indicates for the gap at the valley between FTO layer and TiO$_2$ blocking layer),and (e) IV curves of PSCs with MS-TiO$_2$, and SG-blocking layers [21].

that to improved TiO$_2$ layer can effect to the electron collection and effective hole blocking. Nevertheless, increasing time from 35 to 60 min corresponding to the thickness from 80 to 200 nm, the decreased device performance. When the thickness of cp layers increased or longer transmission distance so the recombination rates increased. This can be confirmed from the obvious decrease of FF parameters.

Yanget *et al.* [23] used TiO$_2$ layer from sputtering method to fabricated PSCs. They fabricated TiO$_2$ layer by using DC magnetron sputtering power at 400 W and 3-inch-diameter metallic plate of Ti (99.995%). The sputtering pressure was kept at 7.5×10^{-3} Torr with a mixture gas of Ar and O$_2$. The thickness of TiO$_2$ layer was about 60 - 70 nm. The average efficiency of the PSCs was 15.37%

Mali *et al.* [24] fabricated TiO$_2$ layer with different thicknesses by RF magnetron sputtering, using an area of 2 cm^2 and 99.99% purity of Ti metal target. For sputtering process, the sputtering pressure was at 10 mTorr with flowing Ar and O$_2$ gases during sputtering. And sputtering power was 130 W. The thicknesses were 30, 50 and 100 nm. They found that RF-magnetron sputtered 50 nm-thick TiO$_2$ layer showed a PCE in excess of 15%

In this work, effects of electron transporting layer TiO$_2$ on PSCs were investigated. The TiO$_2$ layers were fabricated by RF magnetron sputtering and spin coating methods with various conditions using Au/spiro-OMeTAD/MAPbI$_3$ and/or mp-TiO$_2$/cp-TiO$_2$/FTO as the PSC structure with the MAPbI$_3$, and spiro-OMeTAD fabricated by spin coating method, and Au electrodes by thermal evaporation.

1.2 Objectives

- To fabricate cp-TiO$_2$ thin films by RF-magnetron sputtering and spin coating techniques and study the effects of deposition parameters on the textures and surface morphologies of TiO$_2$.
- To study effects of TiO$_2$ textures and morphologies on the efficiency of CH$_3$NH$_3$PbI$_3$ perovskite solar cells.
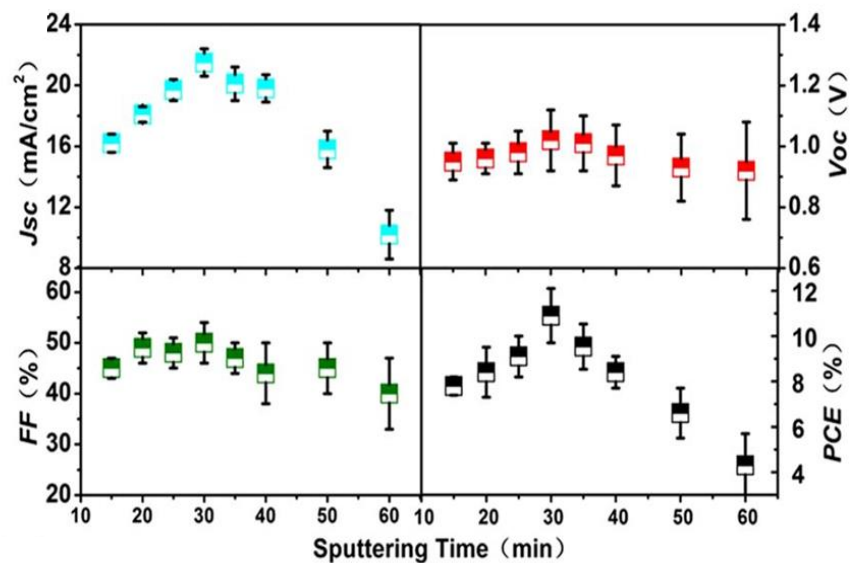
Figure 3 Plots of photovoltaic parameters of the devices based on different sputtering time. 12 solar cells were repeated and measured for each sputtering time [22].

1.3 Thesis outline

In this thesis, it consists of six chapters. First, the theoretical backgrounds of perovskite solar cell and its structure, titanium dioxide and its properties are described in chapter II. The experimental procedures are described in chapter III. For the results, they are divided into two parts; the properties of TiO_2 layers and the performance of perovskite solar cells that are described in chapter IV and chapter V, respectively. The last chapter is the summary of this thesis.

CHAPTER II
MATERIAL PROPERTIES AND FABRICATION METHODS

The depositions of TiO₂, perovskite and related components as well as their properties are described in this chapter. The RF magnetron sputtering, which is the method to deposit TiO₂ compact layer, are explained. In addition, spin coating process, which is the method to fabricate layers of PSCs, is also described.

2.1 Principle of PSCs

A standard configuration of a planar heterojunction perovskite solar cell is shown in Figure 4(a). It consists of a transparent conductive oxides coated glass (photon entrance side), an electron transport material or compact metal oxides, perovskite materials, a hole transport material and a metal electrode. The device comprises three
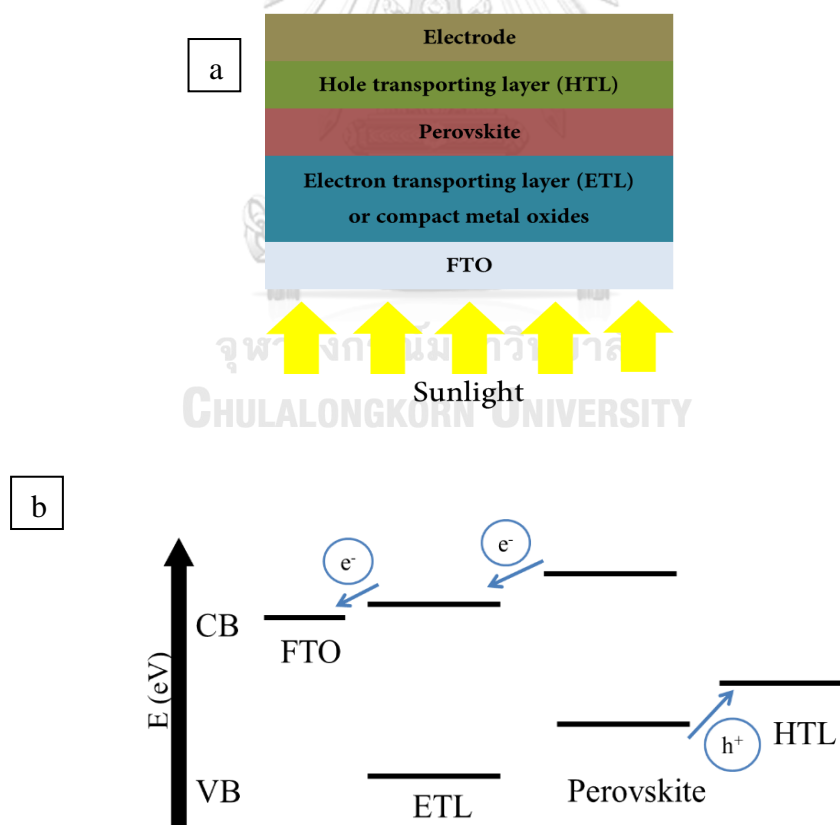
Figure 4 Schematic diagrams represent (a) planar perovskite solar cell and (b) band diagram of PSC.

major components; an absorber to absorb photon, a semiconductor to accept electrons from photo-excited perovskite, and a hole-transporting p–type semiconductor. The working principle of a perovskite solar cell involves a promotion of electrons from the ground state of the perovskite to the excited state upon irradiation with photons and an injection of the excited electrons to the conduction band of the semiconductor. The positive charges on the perovskite are transferred to the hole-transporting material and then to the metal electrode as shown in Figure 4(b). The perovskite plays a critical role in this process for determining the amount of absorbed light both in intensity and wavelength range.

The PSCs typically include the following components;

- Photoanodes

Fluorine-doped tin oxide (FTO) coated glass is electrically conductive and ideal to use in a wide range of devices, including thin film photovoltaics. FTO has been recognized as a very promising material because it is relatively stable under atmospheric conditions, chemically inert, mechanically hard, and high-temperature resistant. It also has a high tolerance to physical abrasion and is less expensive than indium tin oxide (ITO).

- Electron transporting materials (ETM)

For planar PSCs, a compact n-type metal oxide film (for examples, TiO_2, ZnO or SnO_2 [25]) is always required on a transparent conducting oxide (TCO) substrate as a blocking layer for electron selective contacts. TiO_2 ETM has been used in most of the reported PSCs. The electron injection rates from the perovskite absorber to TiO_2 ETM are ultra-fast, but the electron recombination rates are high due to low electron mobility and transport properties [26].

Titanium dioxide (TiO_2) is an n-type semiconductor material that used in several applications, such as sensor devices [27], DSSCs [28], and photocatalysis [29]. The main reasons that TiO_2 becomes favored are long-term photostability, non-toxicity, low cost availability of TiO_2 [30]. Moreover, this material is sensitive to UV radiation, with notable transmittance in the visible region over 80% with high refractive index (between 2.5 and 2.7), chemical stability [31] and band gap of ≥ 3 eV.

TiO$_2$ is used as a photocatalytic material and its photocatalytic activity has been reported in several different studies [32-34]. TiO$_2$ has three crystalline phases: rutile (a tetragonal structure), anatase (a tetragonal structure) and brookite (an orthorhombic structure). At ambient temperature [29], Rutile is the most stable phase. The optical band gap of TiO$_2$ is slightly above 3 eV (rutile: 3.0 eV, anatase: 3.4 eV and brookite: 3.3 eV) [29].

The form of TiO$_2$ used as a photocatalyst under UV radiation is mostly anatase [35]. Rutile has a smaller electron effective mass, higher density and higher refractive index (rutile: 2.609, anatase: 2.488 and brookite: 2.583) [31]. Anatase contains more defects in the lattice, producing more oxygen vacancies and capturing the electrons [36]. Anatase and rutile are generally used in photocatalytic applications, while brookite is not.
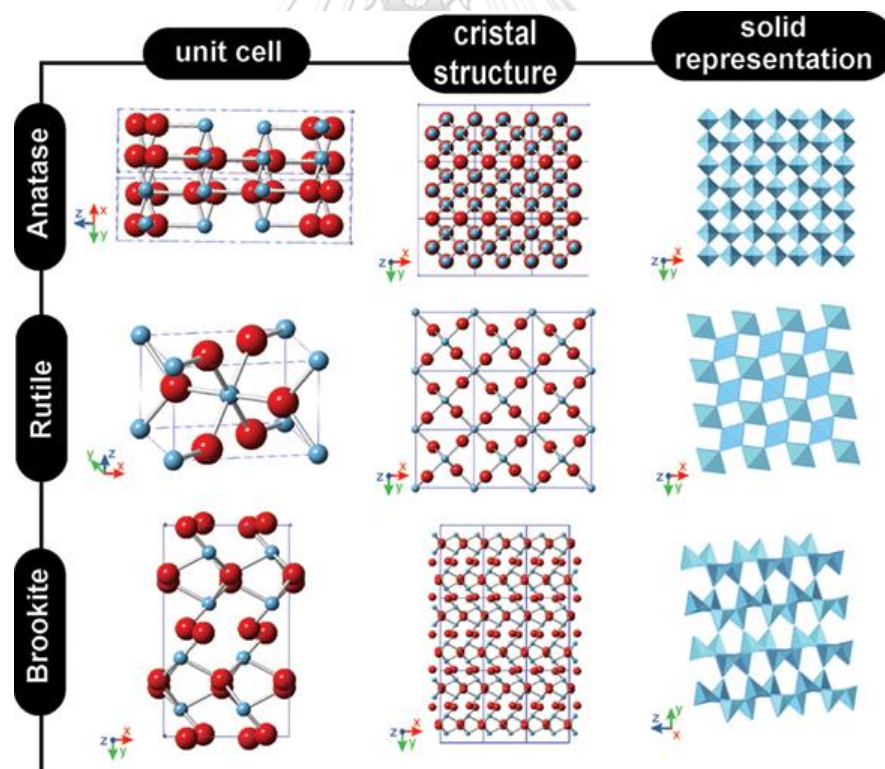
Figure 5 Pictures of crystallographic structures of different TiO$_2$ crystal phases: anatase, rutile and brookite [37].

- Perovskite absorber layer

Methylammonium lead iodide ($CH_3NH_3PbI_3$ or $MAPbI_3$) is one of perovskite materials commonly used to fabricate the solar cells. The effective absorption coefficient of $MAPbI_3$ is around 1.0×10^5 $(mol \cdot L^{-1})^{-1}cm^{-1}$ at 550 nm [38, 39]. $MAPbI_3$ can completely absorb light, when the thickness of the layer is 500 – 600 nm. The diffusion lengths of the electrons and holes in $MAPbI_3$ are 130 nm and 100 nm, respectively [40].

- Hole transporting materials (HTM)

The PSCs typically employ a wide variety of organic polymer hole conductors, e.g. PMMA, Spiro-OMeTAD, PCBM, etc. One of the most notable hole conducting polymers is spiro-OMeTAD [10]. The trade-off between the series and shunt resistance in PSCs is controlled by the performance of perovskite and/or HTM [41]. It is well known that perovskite is highly conductive, on the order of 10^{-3} S cm^{-1}, which requires a thick layer of HTM to avoid pinholes. Spiro-OMeTAD are less conductive ($\sim 10^{-5}$ S cm^{-1}) and its thicker capping layer results in high series resistance [13]. It is indisputable that the HTMs play an important role in PSCs.

- Metal electrode

For PSCs, gold is used to make an electrode, and usually made by thermal evaporation or sputtering technique. Some metal electrodes such as aluminum can induce degradation in PSCs while gold can preserve the stability of the PSCs.

2.2 Deposition methods

2.2.1 Deposition of TiO_2

There are many methods that can be used to deposit TiO_2 layer such as aerosol spray pyrolysis [14-16], thermal oxidation [17], spin-coating method [18], atomic layer deposition[19], and electrochemical deposition [20]. In this work, RF magnetron sputtering and spin coating methods are used to deposit cp-TiO_2 layer.

RF magnetron sputtering process

The process of basic sputtering is such that a target of material desired to be deposited is bombarded with energetic ions such as Argon (Ar^+). These inert gas ions collide onto the target and remove target atoms and then these atoms condense on the substrate as a thin film. The process is limited by low deposition rates, high substrate heating and low ionization efficiencies. Therefore, magnetron sputtering was developed to solve these limitations.

Magnetron sputtering is an effective process for deposition of a wide range of thin film materials. This process utilizes a strong magnetic field near the target area, which causes the travelling electrons to spiral along magnetic flux lines near the target. This arrangement confines the plasma near the target area without causing the damage to the thin films being formed on the substrate. Moreover, in an RF magnetron sputtering systems, the generated electrons travel a longer distance, hence increasing the probability of further ionizing the inert gas atoms (Ar^+) and generating stable high-density plasma that improves the sputtering process efficiency [42].

The reactive sputter deposition process is a process that when a reactive gas such as oxygen is added to the sputtering process. The O_2 gas can react with the sputtered metal atoms on the substrate to form a metal oxide layer. Figure 6 shows the reactive sputter deposition process. Oxygen atoms, originating from plasma reactions with the O_2 gas (a), or from sputtering the poisoned TiO_x target (b), as well as O_2 gas molecules, can react with sputtered Ti atoms on the substrate to form a TiO_x film.
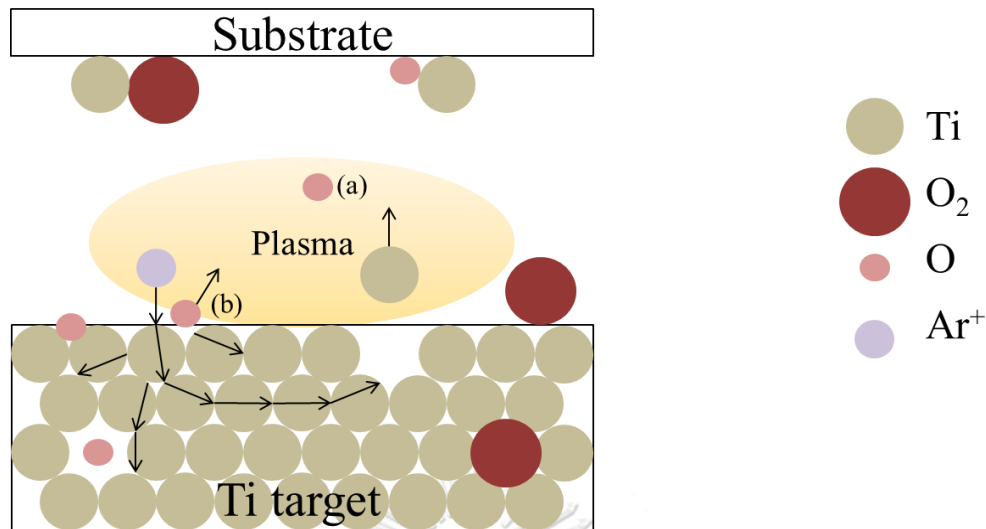
Figure 6 Schematic diagram representing the reactive sputter deposition process; O atoms originating from plasma reactions with the O_2 gas (a), or from sputtering the poisoned TiO_x target (b), as well as O_2 gas molecules can reacting with sputtered Ti atoms on the substrate to form a TiO_x film.

Spin coating process

Spin coating has been used for several decades for the application of thin film deposition. For this process, the substrate is first coated with a solution and then spun at high angular speed. Centripetal acceleration will cause the solution to spread out, and eventually off the edge of the substrate, leaving a thin film of solution on the surface. Properties and film thickness depend on the nature of the solution such as viscosity, drying rate, percent solids, surface tension, etc. Moreover, it depends on the parameters chosen for the spin process. Spin speed is one of the most important factors, because it can affect the film thickness. The film thickness is proportional to the inverse of the square root of spin speed,

$$t \propto \frac{1}{\sqrt{\omega}} \ , \tag{1}$$

where t is the thickness and ω is the angular velocity.

Furthermore, acceleration can affect the uniformity of coating. Since the solution begins to dry during the first part of the spin cycle, it is important to accurately control the acceleration. Moreover, fume exhaust can also affect the film. The drying

rate of the fluid during the spin process depend on the nature of the fluid and the air surrounding the substrate during the spin process such as air temperature and humidity [43].

2.2.2 Deposition processes for perovskite films

There are many techniques to fabricate perovskite layers, e.g. one-step precursor deposition (OSPD), sequential deposition process (SDP), two step spin-coating deposition (TSSD), dual source vacuum deposition (DSVD), sequential vapor deposition (SVD), vapor-assisted solution process (VASP) and spray-coating deposition (SCD) [44].
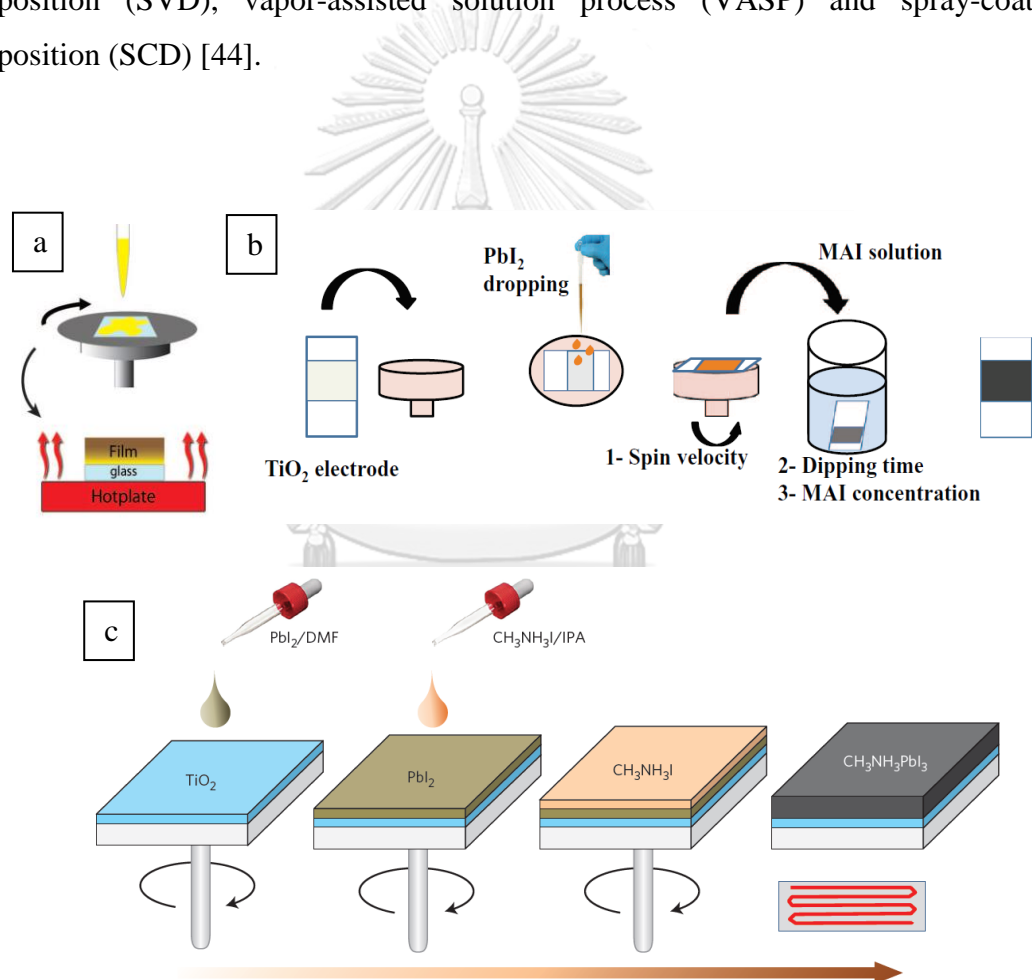
Figure 7 Schematic diagrams of solution-based deposition methods (e.g. MAPbI₃); (a) one step precursor deposition (OSPD) [45], (b) sequential deposition process (SDP) [46], and (c) two step spin-coating deposition (TSSD) [47].

2.1.1.1 Solution-based deposition methods (OSPD, SDP, TSSD, SCD)

Figure 7(a) shows the one step precursor deposition for perovskite layer, which is a spin-coating of a mixture between MAX and PbX_2 (X = halide group) to form perovskite film on the substrate. Changing the precursor concentration or spin speed can be used to control the thickness of a coating layer.

Figure 7(b) is the sequential deposition process. First spin with PbX_2 solution on the top of substrates and follow by dipping it into a solution of MAI in 2-propanol to transform into perovskite.

Figure 7(c) depicts the two-step spin-coating deposition method. For this technique, PbI_2 and MAI solutions are spin-coated sequentially on the substrate and followed by thermal annealing at 100°C to drive the inter-diffusion of precursors to a perovskite layer.

2.1.1.2 Vapor-based deposition methods (DSVD, SVD, VASP)

Vapor-based deposition methods are not commonly used to fabricate perovskite because the process requires have high cost equipment and as well as complex procedures.

Figure 8(a) is a schematic diagram of the process using dual sources vacuum deposition, i.e. MAX and PbX_2 are evaporated from two separate heating sources.

Figure 8(b) is a process of sequential vapor deposition. In this process, PbX_2 and MAI are vapor-deposited on the substrates layer by layer. PbX_2 reacts with MAI in situ, followed by thermal annealing to complete the perovskite crystal transformation.

Figure 8(c) shows the process of vapor-assisted solution. In this process, first spin with PbI_2 solution, then the PbI_2-coated substrates are annealed in MAI vapor at 150°C in N_2 atmosphere. After cooling down, the as-prepared substrates are washed with isopropanol, dried and annealed to complete the deposition.
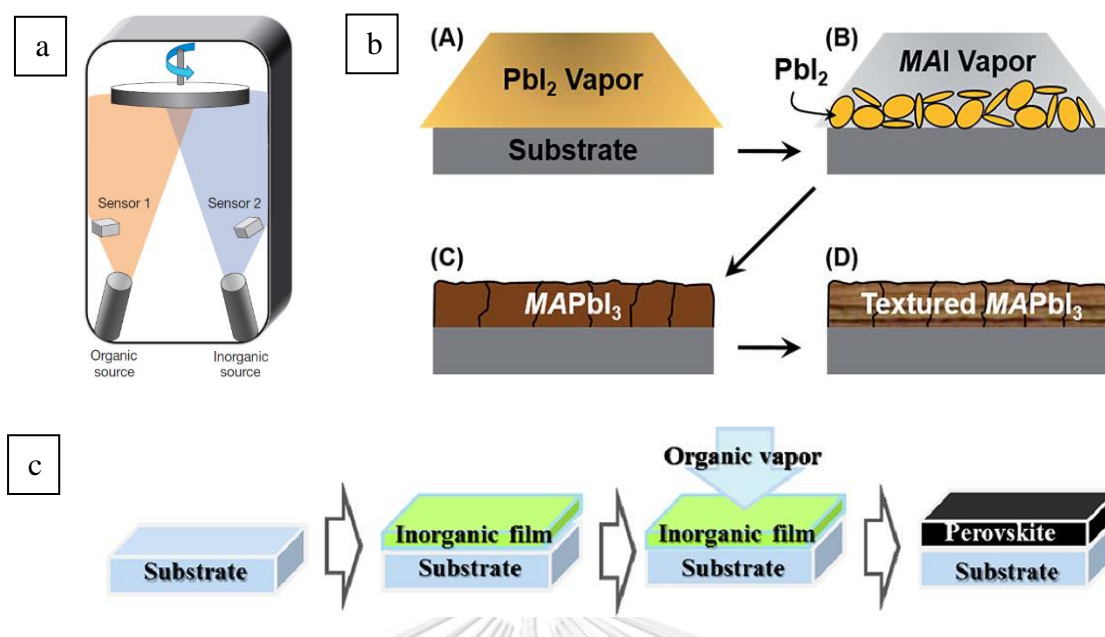
Figure 8 Schematic diagrams of vapor-based deposition methods; (a) Dual source vacuum deposition (DSVD) [48], (b) Sequential vapor deposition (SVD) (e.g. MAPbI₃) [49], and (c) Vapor assisted solution process (VASP) [50].

CHAPTER III

FABRICATION AND CHARACTERIZATION OF TiO₂ AND PEROVSKITE SOLAR CELLS

In this chapter, the fabrications of the TiO₂ and perovskite solar cells are described. The characterization techniques, such as field-emission scanning electron microscopy (FESEM), UV-VIS-NIR spectrophotometer, current-voltage (I-V) measurements, x-ray diffraction (XRD) and atomic force microscopy (AFM) were used to investigate the properties of TiO₂ thin films and the perovskite solar cells (PSCs).

3.1 Fabrication processes of PSCs

3.1.1 Substrate preparation

In this work, 3.0 cm × 3.0 cm FTO coated glasses with thickness of 3 mm were used as the substrates for the deposition of TiO₂ compact layers. The thickness of FTO layer was approximately 800 nm. To avoid a short circuit, the FTO layer was patterned or etched by covering the substrate with a 2.0 cm × 3.0 cm polyimide tape to protect the underlying FTO. The uncovered area was spread with a thin layer of zinc-powder. A few drops of hydrochloric acid (HCl) were added in order to etch the FTO-layer. Then the polyimide tape was removed and left with the remaining FTO as shown in Figure 9.
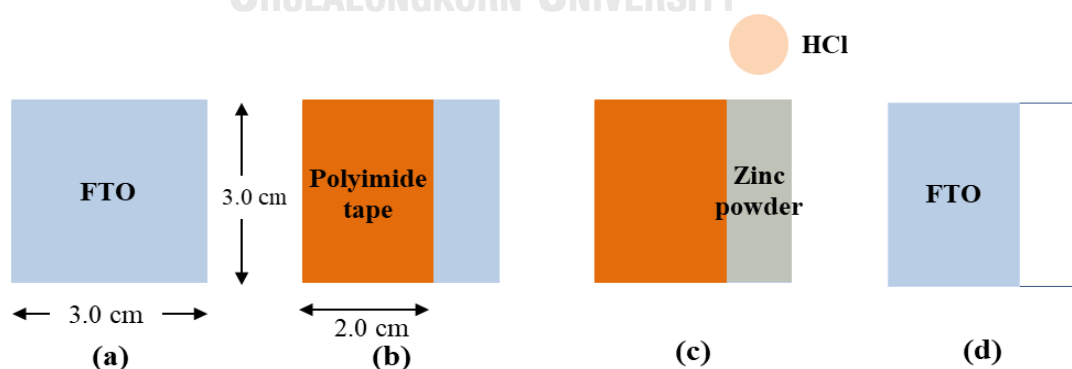
Figure 9 Schematic diagrams representing (a) 3.0 cm × 3.0 cm FTO coated glasses, (b) FTO coated glass covered by 2.0 cm × 3.0 cm polyimide tape, (c) covered with a thin layer of zinc-powder on (b) and adding HCl, and (d) Patterned-FTO conductive glasses.

The patterned-FTO conductive glasses were then cleaned in an ultrasonic bath filled with detergent diluted in deionized (DI) water, DI water, acetone, and methanol sequentially for 15 minutes each. Finally, they were rinsed with DI water and blown dry with N_2 gas. Then, the substrates were kept in a humidity-reduced container.

3.1.2 Deposition of TiO_2 compact layers

TiO_2 compact layers in this work are deposited by RF magnetron sputtering and spin coating methods.

3.1.2.1 RF magnetron sputtering of TiO_2 compact layers

The compact TiO_2 blocking layers were deposited by RF magnetron sputtering onto the FTO coated glasses using a (4-inch diameter) Ti metallic target with a target-to-substrate distance of 60 mm. Stainless steel foil with 1.4 cm × 1.4 cm opening area was used as a shadow mask to define an active area of the PSCs as shown in Figure 10 (b). The base pressure before the deposition was 3.0×10^{-6} mbar. High purity oxygen (99.999% purity) and argon (99.999% purity) gases were used as the sputtering gas. During the deposition, the substrates were loaded in a carousel and rotated above the target at the rate of 5 rpm. The TiO_2 layers were fabricated with $O_2/(O_2+Ar)$ ratios of 30% and 50%, RF power from 100 W to 250 W, deposition time from 120 to 240 minutes, and finally annealed at 500ºC for 1 hour in ambient air. The total sputtering gas pressure was approximately 1.1×10^{-3} mbar.
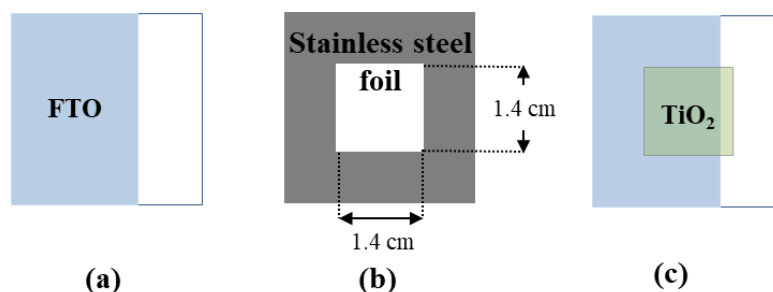
Figure 10 Schematic diagrams representing (a) a cleaned patterned-FTO, (b) a stainless steel foil mask, and (c) a cp-TiO_2 patterned on FTO used in the sputtering process.
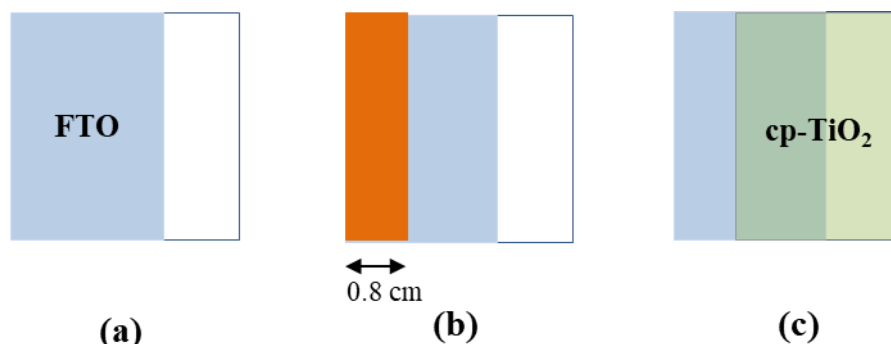
Figure 11 Schematic diagrams representing (a) a cleaned patterned-FTO, (b) a cleaned FTO covered by 0.8 cm × 3.0 cm polyimide tape, and (c) a patterned cp-TiO$_2$ on FTO used in spin coating method.

3.1.2.2 Spin coating of TiO$_2$ compact layers (cp-TiO$_2$)

For the spin coating method, the FTO coated glasses had to be patterned by covering with a polyimide tape to protect the underlying the FTO for making electrodes as shown in Figure 12. The compact TiO$_2$ blocking layers were deposited by spin coating technique onto the FTO coated glasses using a Ti-Nanoxide BL/SP from Solaronix. TiO$_2$ solution (200 µl) was spin-coated on the FTO coated glasses with various speeds for 30 s (without loading time). After spinning, the films were baked at 550°C for 45 minutes on a hot plate.

3.1.3 Deposition of TiO$_2$ mesoporous layers (mp-TiO$_2$)

Ti-Nanoxide T600/SP (Solaronix) containing 15-20 nm titanium dioxide anatase particles was used to fabricate mesoporous TiO$_2$ layer. The substrates were patterned by covering with a polyimide tape and then TiO$_2$ solution (200 µl) was spin-coated on the cp-TiO$_2$ at 5000 rpm for 30 s (without loading time) as shown in Figure 12(b) – (c). After spinning, the films were baked at 475 °C for 30 minutes.
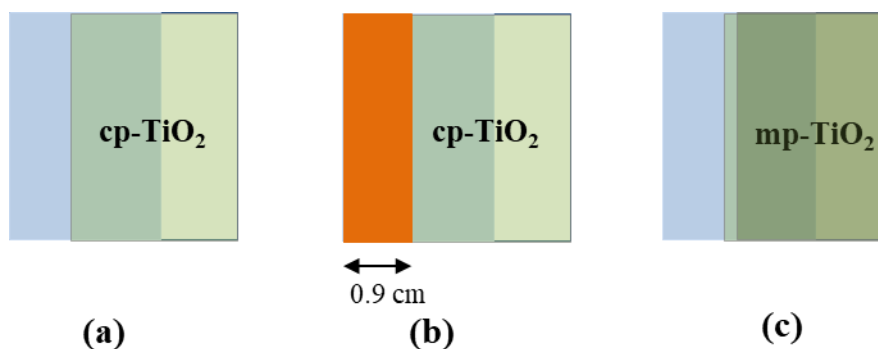
Figure 12 Schematic diagrams representing (a) cp-TiO$_2$ patterned on FTO, (b) a covered 0.9 cm × 3.0 cm polyimide tape on cp-TiO$_2$ patterned on FTO, and (c) a patterned mp-TiO$_2$ layer.
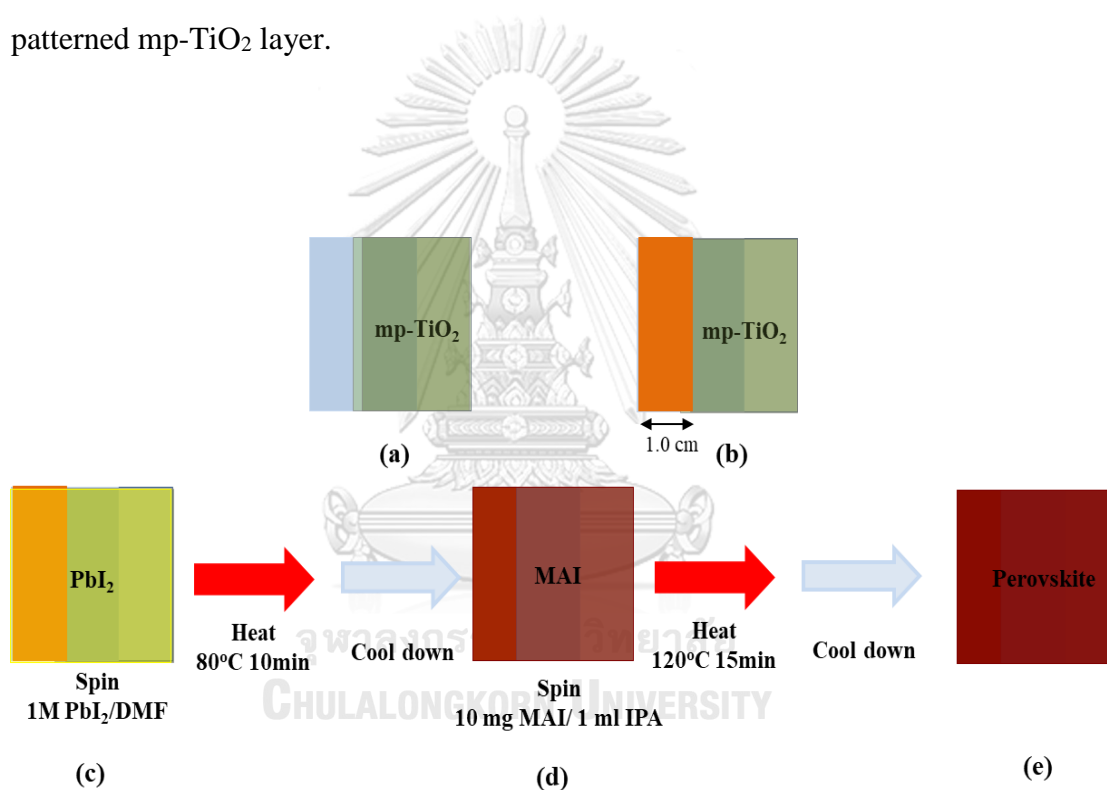
Figure 13 Schematic diagrams representing a two-step spin coating method; (a) a patterned mp-TiO$_2$ layer, (b) a covered 1.0 cm × 3.0 cm area with polyimide tape on mp-TiO$_2$ layer, (c) PbI$_2$ layer deposition by spinning on (b), (d) spinning MAI on (c), and (e) a perovskite layer.

3.1.4 Deposition of perovskite absorber

A $CH_3NH_3PbI_3$ layer was fabricated by using a two-step spin coating method. PbI_2 solution (1 M) was prepared by dissolving 461 mg PbI_2 (99%, Aldrich) in 1 ml N,N-dimethylformamide (DMF, 99.8%, Sigma-Aldrich) and stirred at 80 °C for overnight. Figure 13 shows a two-step spin coating method. First, the patterned mp-TiO_2 layer (Figure 13(a)) was covered by 1.0 cm × 3.0 cm polyimide tape (Figure 13(b)). Then, PbI_2 solution (100 µl) was dispersed and spin-coated on the mp-TiO_2 layer at 3,000 rpm for 30 s (without loading time) (Figure 13(c)). After spinning, the film was baked at 80 °C for 10 min, and left to cool down to room temperature, then 0.063M (10 mg ml^{-1}) CH_3NH_3I solution in 2-propanol was dispersed and spin-coated on the PbI_2 film at 2000 rpm for 10 s and 4000 rpm for 10 s with loading time of 30s (Figure 13(d)), and then dried at 120°C for 15 min to transform into the perovskite (Figure 13(e)).

3.1.5 Deposition of hole transporting layer

Spiro-OMeTAD solution was prepared by dissolving 72.3 mg of spiro-OMeTAD in 1 ml of chlorobenzene, to which 28.8 µl of 4-*tert*-butyl pyridine and 17.5 µl of lithium bis(trifluoromethanesulfonyl)imide (Li-TFSI) solution (520 mg LI-TSFI in 1 ml acetonitrile, Sigma-Aldrich, 99.8%) was added [47]. The Spiro-OMeTAD solution was stirred overnight. The Spiro-OMeTAD solution (100 µl) was spin-coated on the perovskite film at 3,000 rpm for 30 s.
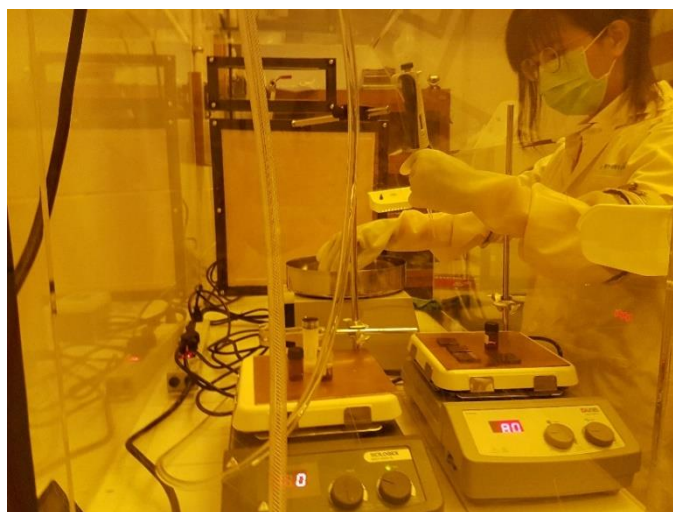
Figure 14 A photograph of the fabrication of PSCs.

3.1.6 Deposition of electrode

Gold (Au) is generally used as an electrode for PSCs. Thermal evaporation was used to fabricate 80-100 nm thick Au through a stainless steel foil shadow mask to make patterns on the surface of Spiro-OMeTAD. The base pressure was about 1.5×10^{-5} mbar prior to the deposition of Au. Since cp-TiO$_2$ layers from sputtering and spin coating methods have different patterns, stainless steel masks are designed differently. Figure15(b) and Figure16(b) show the mask patterns for cp-TiO$_2$ sputtering method and spin coating method.
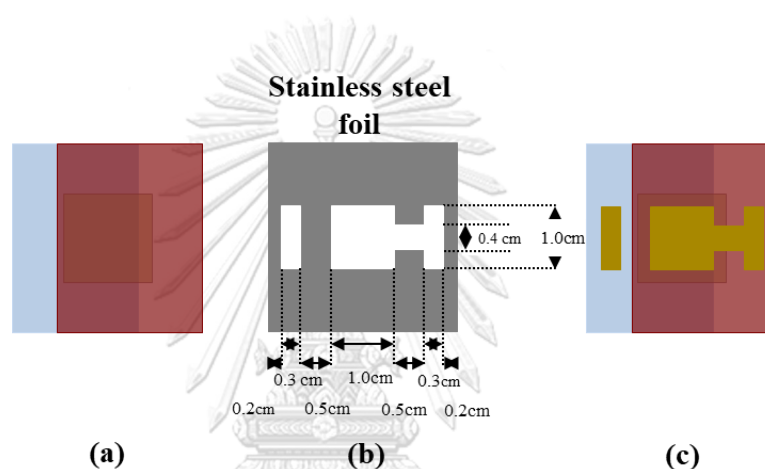
Figure 15 Schematic diagrams representing (a) spiro-OMeTAD/MAPbI$_3$/mp-TiO$_2$/cp-TiO$_2$(sputtering)/FTO, (b) a mask pattern for cp-TiO$_2$ sputtering method, and (c) a PSC with Au contacts.
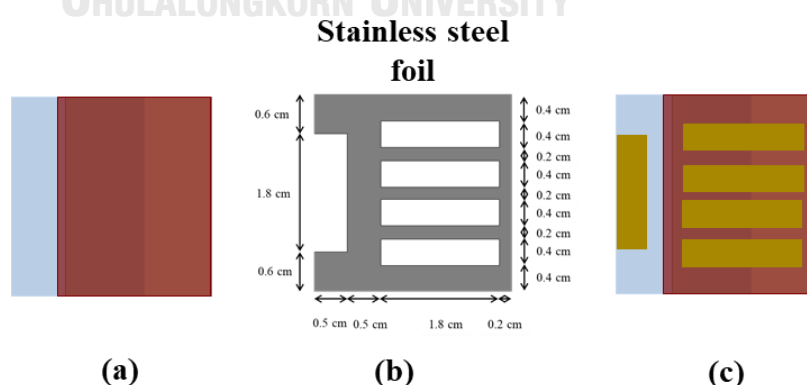
Figure 16 Schematic diagrams representing (a) spiro-OMeTAD/MAPbI$_3$/mp-TiO$_2$/cp-TiO$_2$(spin coating)/FTO, (b) a mask pattern for cp-TiO$_2$ spin coating method, and (c) a PSCwith Au contacts.

Figure 17 A photograph of evaporated Au on PSCs

3.2 Characterization techniques

The characterizations of cp-TiO$_2$ films and the PSCs were performed by I-V measurement, optical transmission spectroscopy, FESEM, AFM and XRD.

3.2.1 Current-voltage (I-V) measurement

When the fabrications of cp-TiO$_2$ layers and the PSCs were complete, they were investigated by the I-V measurements. The I-V measurement set-up consists of a xenon arc lamp and a source-meter unit (Keithley model 238). The devices were analyzed under AM1.5 condition at room temperature (25°C) with the light intensity of 100 mW/cm^2. The data acquisition was run by Agilent VEE program. The parameters of interest for solar cell are open-circuit voltage (V$_{oc}$), short-circuit current density (J$_{sc}$), fill factor (FF) and efficiency which can be determined from the I-V curve.

3.2.2 Field Emission Scanning Electron Microscopy (FESEM)

Surface morphology of TiO$_2$ and its thickness are measured by JEOL JSM 7001 FESEM. It is used to study microstructures or nanostructures of all layer in PSCs. In this study, the surface morphology is imaged at X10,000, X20,000, X30,000 and X50,000 magnifications.
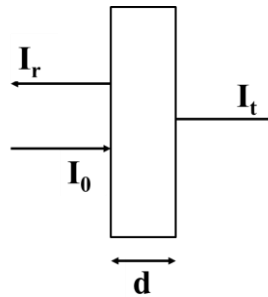
Figure 18 Schematic diagram of optical transmission and reflection in thin film.

3.2.3 Optical transmission spectroscopy

The optical absorption and transmission properties of cp-TiO$_2$ and perovskite thin film were characterized by the Perkin-Elmer Lambda 900 UV-VIS-NIR spectrophotometer in the wavelength from 300 nm to 1800 nm.

3.2.3.1 Optical absorption properties

Figure 18 shows a schematic diagram of normal incidence of light onto a thin film. The intensities of the incident wave, transmitted wave, and reflected wave are denoted I$_o$, I$_t$, and I$_r$ respectively. The intensity of a light wave (I) in the thin film decrease as

$$I = I_0 e^{-\alpha x}, \tag{2}$$

where x is the thickness of thin film and α is the absorption coefficient. The transmission (T) and the reflection (R) can be expressed in terms of

$$T = \frac{I_t}{I_0} , \tag{3}$$

$$R = \frac{I_r}{I_0} . \tag{4}$$

From Equations 3 and 4 the optical absorption coefficient can be obtained from

$$\alpha = \frac{1}{d} \ln \left(\frac{I_0}{I_t} \right) . \tag{5}$$

In the absorption process, a photon can excite an electron from lower-energy (valence band) to higher-energy state (conduction band). This is called an interband transition and it can be divided into the following cases [51]:

Allowed direct transition: $\alpha(h\nu) = \frac{A}{h\nu}\left(h\nu - E_g\right)^{1/2}$,   (6)

Forbidden direct transition: $\alpha(h\nu) = \frac{B}{h\nu}\left(h\nu - E_g\right)^{3/2}$,   (7)

Indirect transition: $\alpha(h\nu) = \frac{C}{h\nu}\left(h\nu - E_g\right)^{2}$,   (8)

where A, B, C are the constants, $h\nu$ is the photon energy, and E_g is the energy gap of the semiconductor. From Equations 5 and 6, the energy gap is obtained from the extrapolation from the linear section of the plot between $(\alpha h\nu)^2$ and hv.

3.2.4   Atomic force microscopy (AFM)

The surface roughness of TiO_2 films can be analyzed by AFM technique. An AFM uses the van der Waals force between atoms to generate the surface morphology of the sample. Figure **19**Figure 19 shows the basic scheme of AFM. It consists of a microfabricated flexible cantilever with one or multi-tips, a photo-sensitive detector and a feedback loop for detection. When the probe moves along the sample surface, the deformation changes or movements of the cantilever are simultaneously recorded. The vertical bending of the cantilever is measured by a photo-sensitive detector [52].
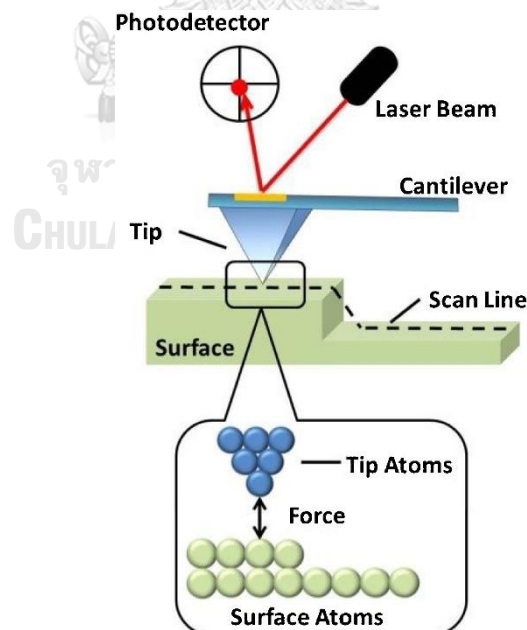

Figure 19 The basic scheme of atomic force microscopy. When the tip scans through the sample, the topography information is recorded by the photodetector, due to the changes of cantilever bending [52].

The surface roughness value shows the total roughness of sample surface which is calculated via the root mean square (rms) method. It can be measured by a statistical analysis method. The distances between the highest and the lowest surface positions are given as z-range. The definition of surface roughness and z-range are shown by following equations,

$$\text{rms} - \text{roughness} \left(R_q \right) = \sqrt{\frac{\Sigma_{i=1}^{N}\left(h_i - \bar{h}\right)^2}{N}} , \qquad (9)$$

where h_i is the height at position i th, $\bar{h}$ is the average height, and N is the number of data points;

$$z - \text{range} = h_{max} - h_{min} , \qquad (10)$$

where h_{max} is the maximum height of sample surface (nm) and h_{min} is the minimum height of sample surface (nm).

In this work, the AFM (Veeco Dimension 3100) with tapping mode was used to study morphology of TiO_2 layers. Tapping mode in AFM is a technique that maps topography by lightly tapping the surface with an oscillating probe tip. The cantilever's oscillation amplitude changes with sample surface topography, and the topography image is obtained by monitoring these changes and closing the z feedback loop to minimize them. The size of scanning images is 5 µm × 5 µm, and the resolution of rms-roughness values is about 1 nm. Moreover, the AFM images are shown in 2 types which are the height image (z) and the phase image $(\frac{dz}{dx})$ – the spatial derivative of the height image along the scan direction.

3.2.5 X-ray diffraction (XRD)

To determine the crystallographic structure of TiO_2 layer, the Bruker D8 Advance X-ray diffractometer (Figure 20) was employed. When the beam of X-rays is incident on a sample, it is diffracted from the crystal plane following the Bragg's law. The path difference shows in Figure 21 related to the distance of each crystal plane (d) [53].

$$2d_{hkl} \sin \theta = n\lambda, \qquad (11)$$

where d_{hkl} is the inter-planar spacing of the crystal plane,

  θ is the Bragg's angle,

λ   is the wavelength of x-ray,

and   n   is equal to one for the first order of diffraction.
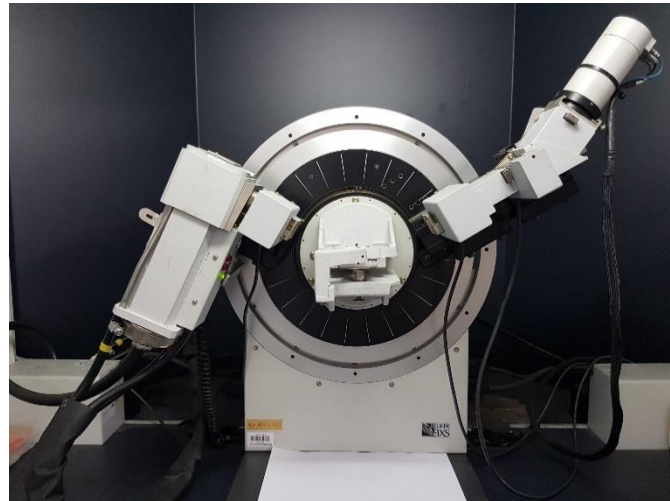
Figure 20 Photograph of Bruker D8 Advance X-ray powder diffractometer.
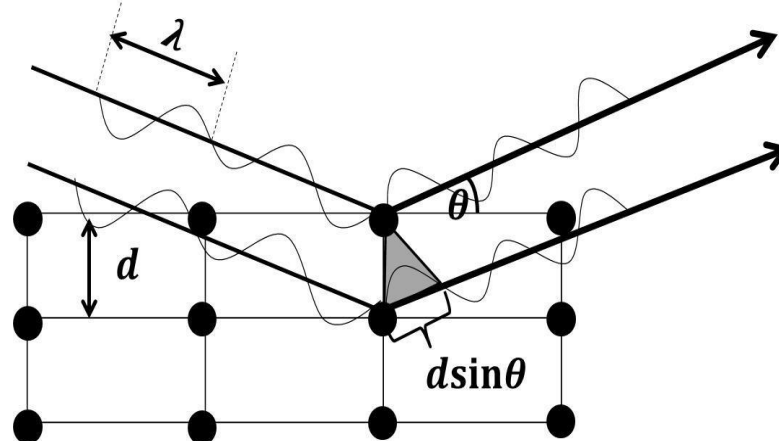
Figure 21 Schematic diagram represents the diffractometer for crystal analysis [54].

CHAPTER IV
RESULTS AND DISCUSSION OF TiO$_2$ LAYERS

In this chapter, the results of TiO$_2$ compact layers fabricated by sputtering and spin coating methods are discussed in terms of electrical properties, I-V characteristics, optical transmission, crystal structure, surface morphology, and rms roughness.

4.1 Electrical properties and morphology of FTO substrate

The thickness of the FTO layer is approximately 800 nm that was measured by using the cross-section FE-SEM images (Figure 22(b)). The resistivity and the carrier concentration at 300 K of the FTO film are approximately $6.5 \times 10^{-4} \Omega \cdot$ cm and $3.7 \times 10^{20} \text{cm}^{-3}$, respectively, as measured by the van der Pauw technique (using Keithley 237 source-measure unit, Keithley 196 DMM, Agilent 34970A DAQ/Switch unit and 1 Tesla electromagnet). This FTO has carrier concentration greater than 10^{20}cm^{-3} which is considered as a heavily doped semiconductor.

The transmittance of the FTO film is above 80% with respect to air in the visible – NIR range and rapidly drops when the wavelength is greater than 1,300 nm as shown in Figure 23 due to free carrier absorption nature of the heavily-doped semiconductor.
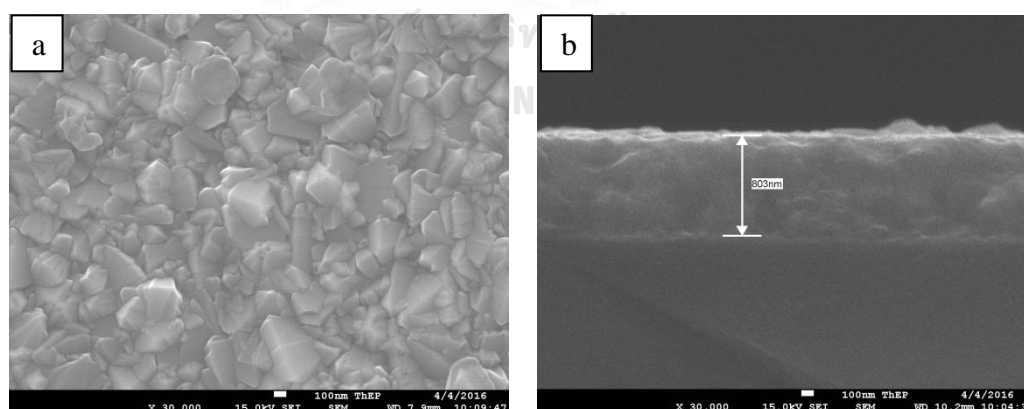
Figure 22 FE-SEM images of (a) surface morphology and (b) cross-section of FTO coated glass.
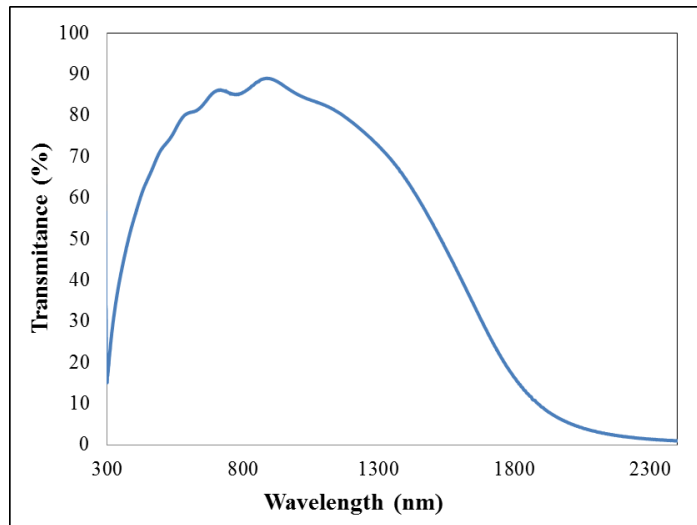
Figure 23 A graph of transmittance of FTO coated glass.

4.2 Characteristics of cp-TiO$_2$ layer from sputtering method

4.2.1 Dark I-V characteristics of TiO$_2$/FTO

Since the carrier concentration in the FTO layer is very high (heavily doped), one may consider it as a good transparent conductor, i.e. the TiO$_2$/FTO interface could be considered as a semiconductor – metal contact.

To find the suitable sputtering condition for the TiO$_2$ film as an electron transport layer, first the RF sputtering power was varied from 100 W to 250 W by maintaining the O$_2$/(O$_2$+Ar) ratio at 30% and the sputtering time of 120 minutes. The results from the I-V characteristics of TiO$_2$/FTO interface (Figure 24) show that the resistance between the TiO$_2$/FTO interface deviates from an ohmic contact towards a diode behavior and thus the current is blocked in the reverse bias when the sputtering power is increased. A good film coverage is obtained when the sputtering power is increased and results in a better semiconductor – metal interface. For the 200 W and 250 W sputtering power, the I-V curves show vanishing current leakage for the reverse bias. This suggests that the TiO$_2$ layers act as hole blocking layers.

Figure 24 A plot of I-V characteristics of TiO_2/FTO interface with different RF power; $O_2/(O_2+Ar)$ ratio = 30%, sputtering time = 120 minutes.
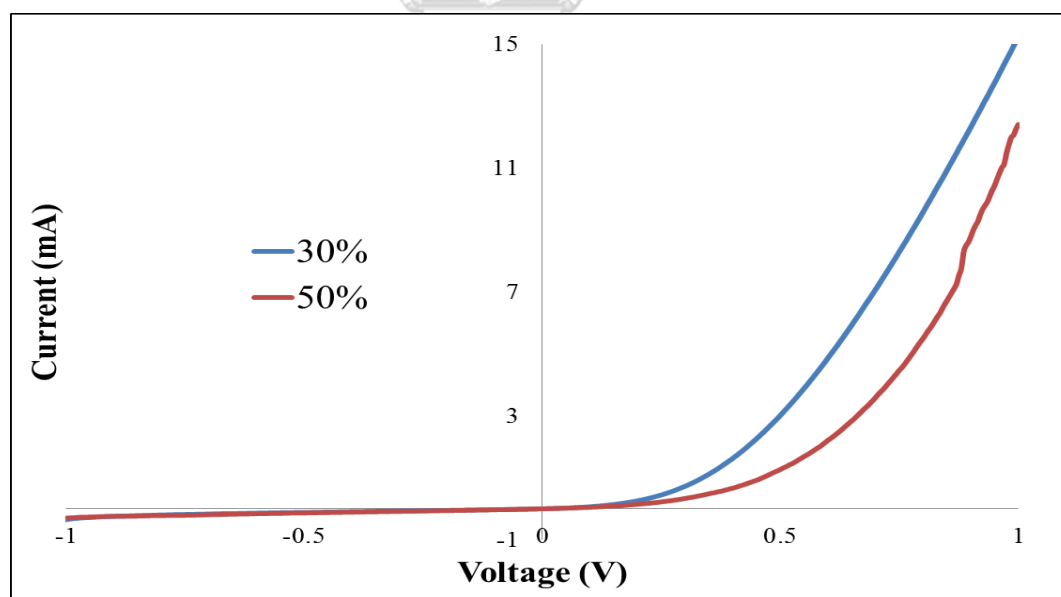
Figure 25 A plot of I-V characteristics of TiO_2/FTO interface with different $O_2/(O_2+Ar)$ ratios, sputtering power = 200W, sputtering time = 120 minutes.

Next the effect of 30% and 50% $O_2/(O_2+Ar)$ ratio are considered from the I-V characteristics of TiO_2/FTO interface using 200 W spu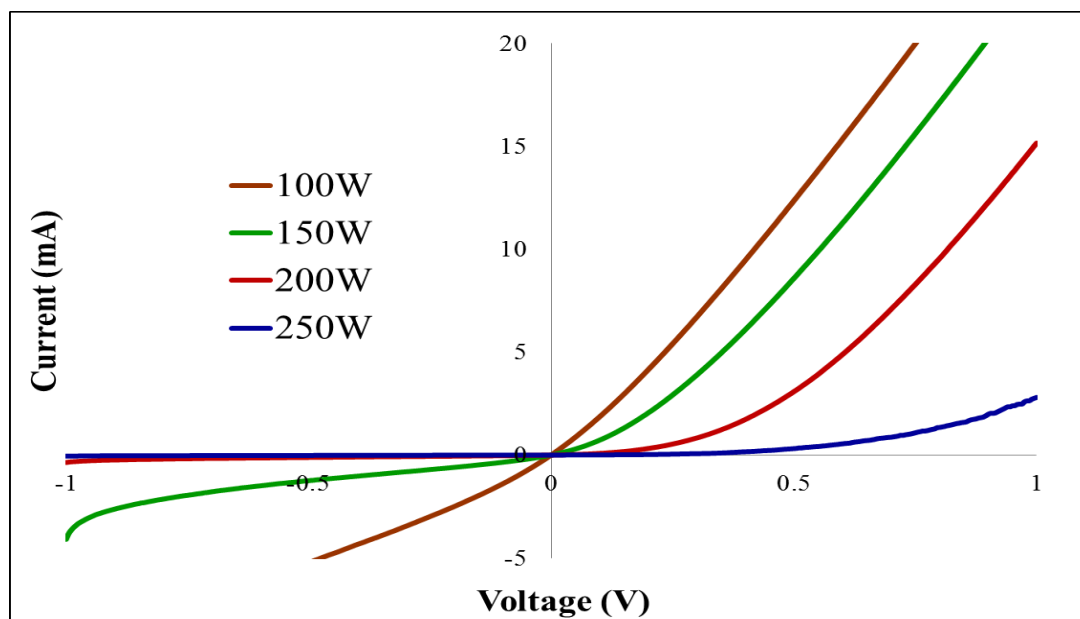ttering power and 120 minutes sputtering time (shortest deposition time). The results in Figure 25 show that series resistance from 50% of $O_2/(O_2+Ar)$ ratio is less than that from 30% of $O_2/(O_2+Ar)$ ratio. It can be inferred that 50% of $O_2/(O_2+Ar)$ ratio sputtering condition is better than 30% of $O_2/(O_2+Ar)$ ratio. Different $O_2/(O_2+Ar)$ ratios can cause different crystal structures due to transport process of the sputtering particles between the substrate and the Ti metallic target [55].

Figure 26 shows the I-V characteristics of TiO_2/FTO interface with different deposition time from 120 to 240 minutes. For the sputtering time from 210 to 240 minutes, there is no current leakage for the reverse bias. Some small current leakage for reverse bias is observed with the sputtering time from 120 to 180 minutes. However, the samples with the sputtering time from 120 to 180 minutes have a trend of higher series resistance than those of the sputtering time from 210 to 240 minutes.
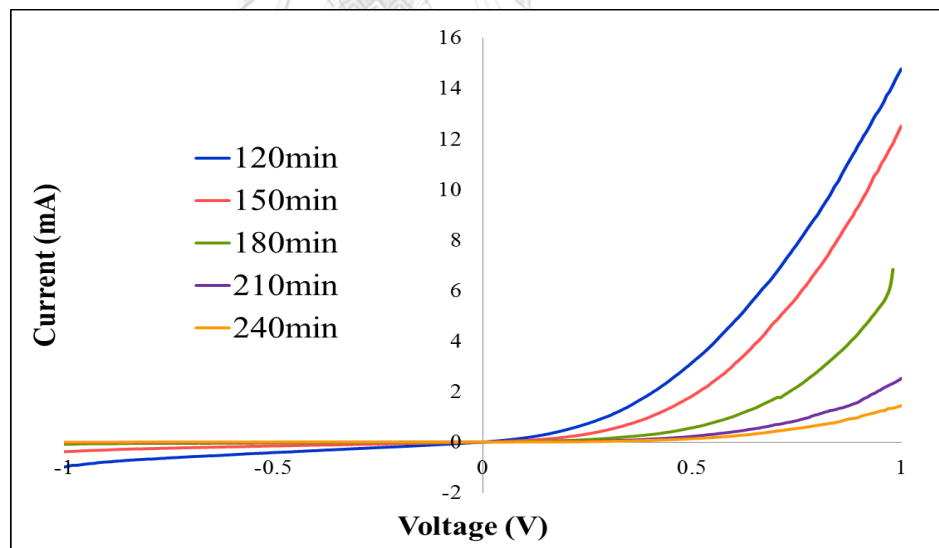
Figure 26 A plot of I-V characteristics of TiO_2/FTO interface with different deposition time, $O_2/(O_2+Ar)$ ratio = 50%, sputtering power = 200W.
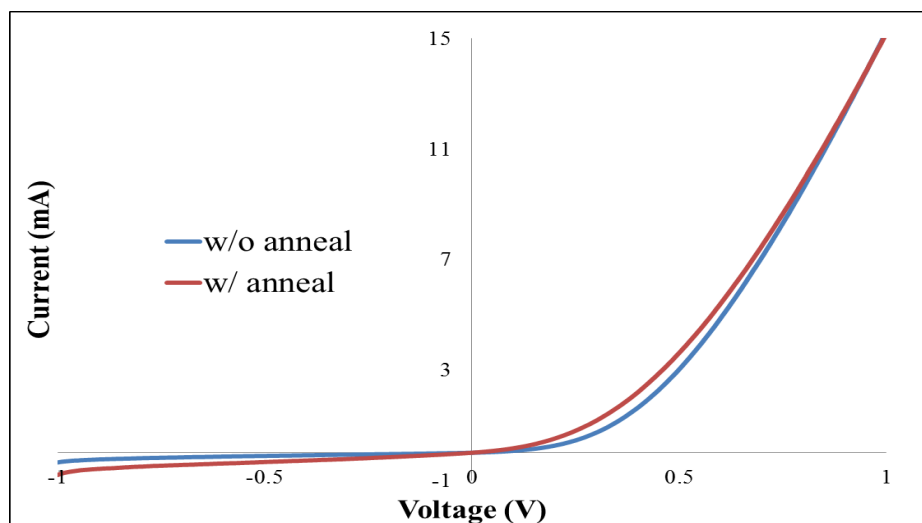
Figure 27 A plot of I-V characteristics of TiO_2/FTO interface with and without annealing at 500°C for 30 minutes in ambient air, O2/(O2+Ar) ratio = 50%, sputtering power = 200W, sputtering time = 120 minutes.
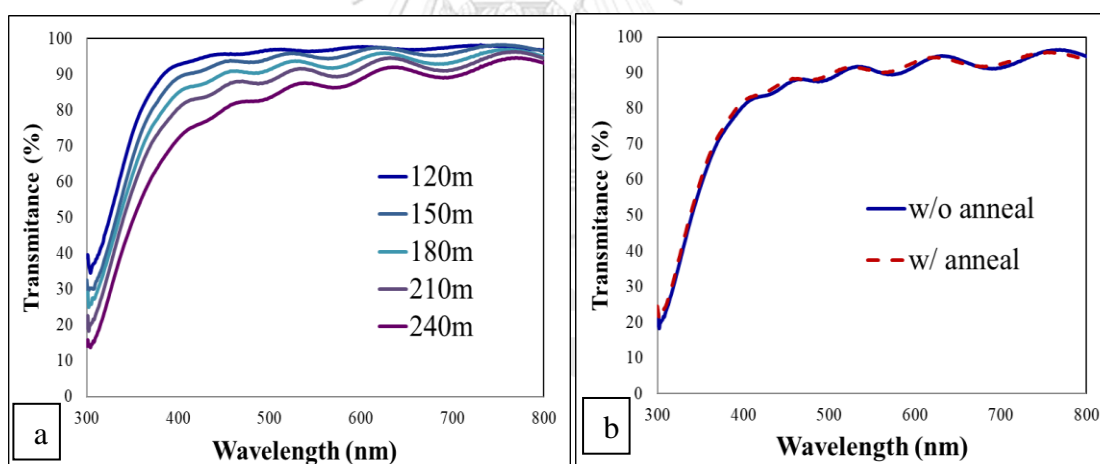
Figure 28 Plots of transmittance of compact TiO_2 layers on FTO coated glasses; (a) with different deposition time and (b) with and without annealing.

For the effect of annealing process, the I-V characteristics of TiO_2/FTO interface with and without annealing at 500°C for 30 minutes from the sample of 50% of O_2/(O_2+Ar) ratio, 200 W sputtering power and sputtering time of 210 minutes are shown in Figure 27. There is a slightly increase in both current leakages in the reverse bias and the series resistance in forward bias for the annealed sample.

4.2.2 The optical transmission of the TiO$_2$ layers

The optical transmission of the TiO$_2$ layers was measured by the UV-VIS-NIR spectrophotometer. Figure 28(a) shows the transmittance of compact TiO$_2$ layers on the FTO coated glasses sputtered at 50% of O$_2$/(O$_2$+Ar) ratio and RF-power of 200 W with different deposition time from 120 to 240 minutes. It is noted that the transmittance measurement of the TiO$_2$ compact layer was normalized with the FTO/glass substrates. When deposition time increases, the transmission decreases due to thicker TiO$_2$ film as expected. The average transmittance of the TiO$_2$ layers is above 80% in the visible regions. In addition, annealing the film does not affect optical transmission of TiO$_2$ layers as shown in Figure 28(b).

Due to a very low deposition rate of sputtered Ti atoms, the TiO$_2$ films obtained by this technique are very thin. The thickness could not be easily measured by FE-SEM due to the nonconductive substrate. The thickest TiO$_2$ layer obtained from longest deposition time of 240 minutes, RF power of 200 W and 50% of O$_2$/(O$_2$+Ar) ratio was measured by the surface profilometer. The thicknesses of TiO$_2$ with less deposition time are deduced from the deposition rate of the thickest one (1.375 Å/min) and summarized in Table 1.

In addition, the energy gap (E$_g$) of the TiO$_2$ can be calculated from the relationship expressed by Equation (6). The wavelength dependent optical absorption coefficient is determined from the optical transmission spectrum as described in Equation (5); $\alpha(\lambda) = \frac{1}{d}\ln\frac{100}{T(\lambda)}$, where T($\lambda$) is a percentage of optical transmission of the film at the wavelength λ, and d is a thickness of the film. The energy gap is obtained from the extrapolation from the linear section of the plot between $(\alpha h\nu)^2$ and hν, where hν is the photon energy. From the calculation, the TiO$_2$ films deposited using 50% of O$_2$/(O$_2$+Ar) ratio and 200 W has the energy gap about 3.65 ± 0.03 eV which is corresponding to the anatase phase and consistent with other work [56].

Table 1 The thicknesses of TiO_2 with different deposition time.

Sputtering time (min)	Approximated thickness (nm)
120	17
150	21
180	25
210	29
240	33

4.3 Characteristics of cp-TiO_2 layer from spin coating method

4.3.1 Dark I-V characteristics of TiO_2/FTO

      To observe the nature of cp-TiO_2 by spin coating method, first the spin speed was varied from 2000 rpm to 6000 rpm. The results from the I-V characteristics of TiO_2/FTO interface (Figure 29) show that the resistance between the TiO_2/FTO interface deviates from an ohmic contact towards a diode behavior, but all of the results show leakage current for the reverse bias. The magnitude of the leakage current does not show monotonic relationship with spin speed that is likely due to a non-uniformity of the films from the spin coating method.
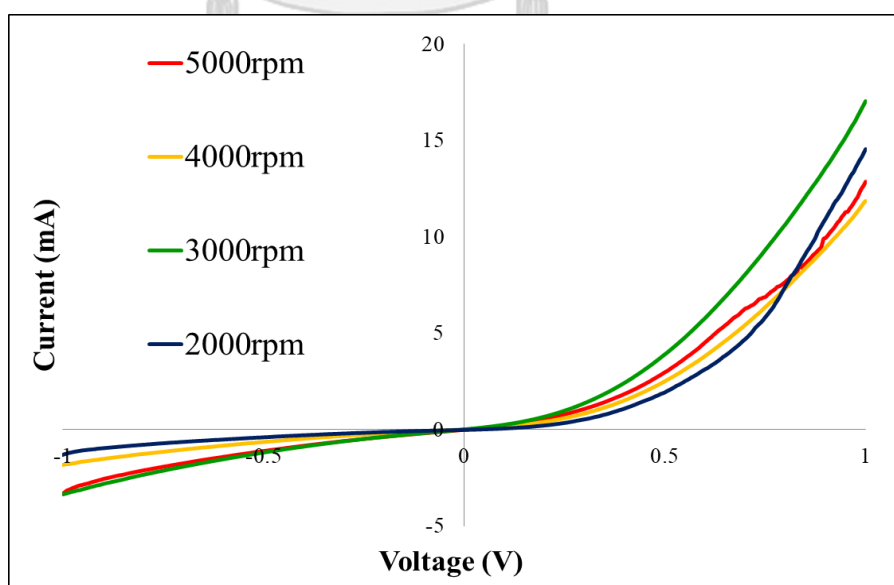
Figure 29 A plot of I-V characteristics of TiO_2/FTO interface with different spin speed from 2000 rpm to 6000 rpm for 30 s.
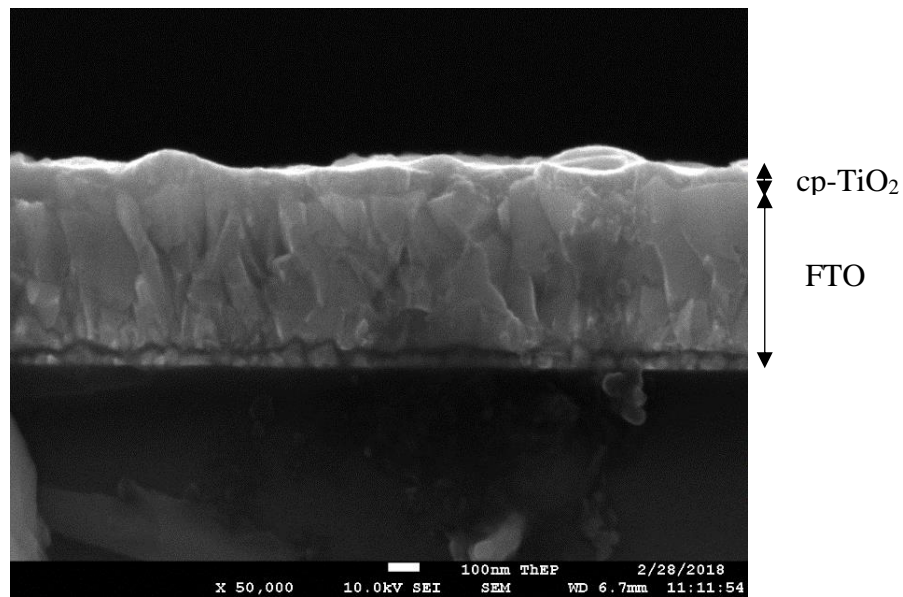
Figure 30 An FESEM image of cross-section of TiO$_2$/FTO for a spin speed 4000 rpm for 30 s.

4.3.2 The thickness of TiO$_2$/FTO

The thicknesses of TiO$_2$ with different spin speed as measured by FESEM, are summarized in Table 2. The energy gap is estimated from the optical transmission measurement to be 3.77 ± 0.02 eV.

Table 2 The thicknesses of TiO$_2$ with different spin speed.

Spin speed (rpm)	Approximate thickness (nm)
2000	78-105
3000	68-99
4000	59-91
5000	54-86
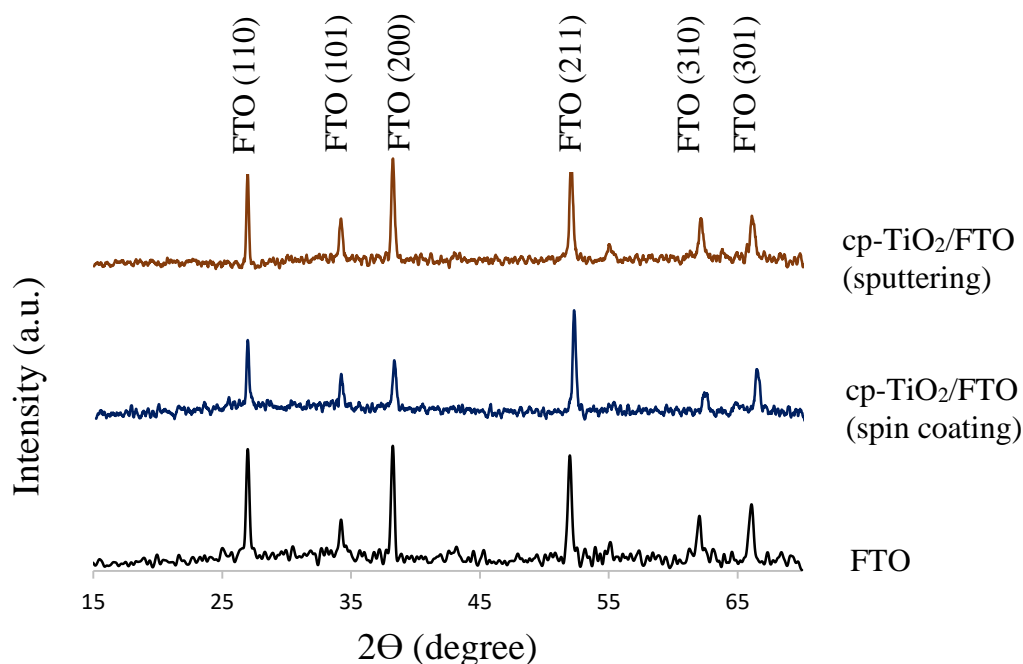
Figure 31 XRD patterns of FTO and cp-TiO$_2$/FTO fabricated by spin coating and sputtering methods.

4.4 Crystal structure

The XRD patterns of FTO and cp-TiO$_2$ fabricated by spin coating and sputtering methods on FTO are shown in Figure 31. The results show that the FTO and FTO coated with cp-TiO$_2$ samples have the same pattern of XRD, i.e. TiO$_2$ peaks do not appear in the XRD results because its layer is very thin for the diffraction intensity to be detected. Therefore, the crystal structure of the very thin TiO$_2$ fabricated by both methods mentioned previously cannot be identified by the XRD measurements.

4.5 Surface morphology and rms roughness

The FESEM and the AFM images of the surfaces of cp-TiO$_2$ on FTO are compared and shown in Table 3. For sputtered TiO$_2$ layers, the FESEM images show no difference between FTO and TiO$_2$/FTO. But the AFM images show that the FTO grains with sharp edges become smoother when coated with TiO$_2$ by the sputtering method. The structure of the grains of TiO$_2$ on FTO is not distinguishable either by

FESEM or AFM. The roughness of the surface of sputtered TiO_2/FTO is close to that of the FTO surface of ~40 – 50 nm as indicated in Table 3.

In order to observe the shape of TiO_2 grains from the sputtering and spin coating methods, the TiO_2 films are deposited on bare soda-lime glass (SLG) substrates and scanned with the AFM. The small round-shape grains of TiO_2 are observed from the sputtering method as shown in Table 4. The roughness of the surface of TiO_2 on SLG is in the order of 20 nm and does not significantly change with the deposition time.

On the other hand, for the spin coated TiO_2 on SLG, the AFM images are relatively blurry in the height (z) images compared to those from the sputtering method. However, when looking at the phase images that represent the rapid change on the surface of the film, one can clearly see small round grains of TiO_2 on the SLG surface as shown in Table 4. In addition, the rms roughness of the TiO_2/SLG by the spin coating method decreases (from ~7 to ~3 nm) as the spin speed increases (from 2,000 to 5,000 rpm) as summarized in Table 4.

Now, when one considers the spin-coated TiO_2/FTO, it is difficult to indicate the existence of TiO_2 layer on the FTO surface via the FESEM, i.e. one can only observe the FTO grains similar to that of the bare FTO surface. On the other hand, the AFM height (z) images become blunt when compared with the images from the sputtering method. In addition, it is shown that the rms roughness is about 20 nm, as indicated in Table 3, which is approximately half of that obtained from the sputtering method. This suggests that the spin-coated TiO_2/FTO which is started with the spread of liquid solution of TiO_2 fills up the valleys on the FTO surface and smoothens out the surface during the spinning of the substrate causing flatter surface as indicated by decreasing of the rms roughness. Moreover, with further investigation, one can observe very small round grains in the phase images of the spin-coated TiO_2 on the FTO grains that is consistent with the shape of TiO_2 grains observed on the SLG substrates.

In summary, the I-V measurements can be used to probe the coating of TiO_2 on FTO substrates by the observation of the diode-like behavior. The morphology or grain shape of the coated TiO_2 on FTO can be identified from the AFM measurement rather than from the FESEM images. The morphology of the sputter-coated TiO_2/FTO is more compact than that of the spin-coated ones. The XRD is not suitable to identify the morphology or the phase of the very thin TiO_2 films (less than 100 nm in this work).

40

Table 3 The FESEM and AFM images of TiO$_2$ on FTO.
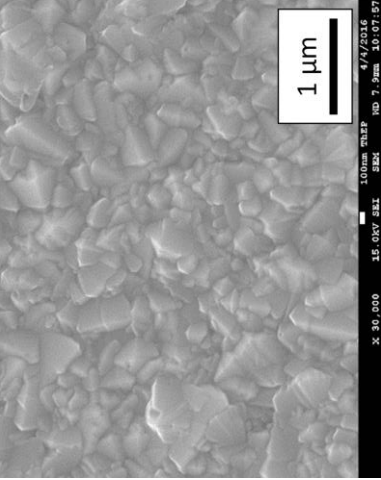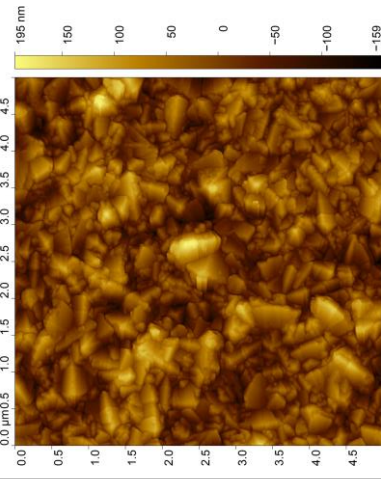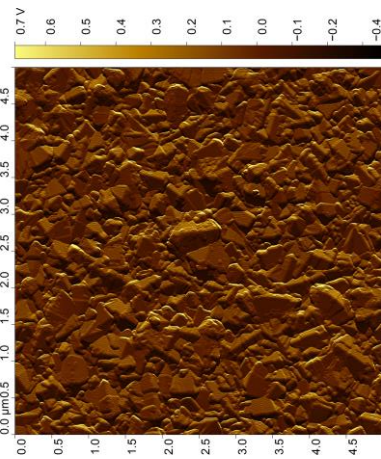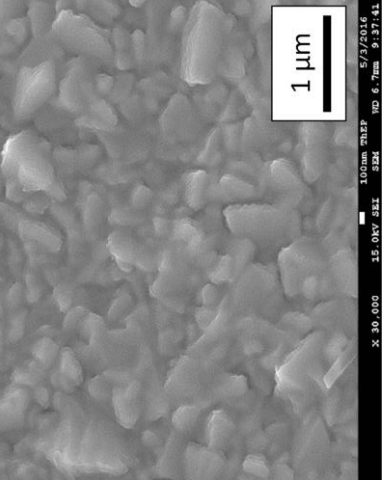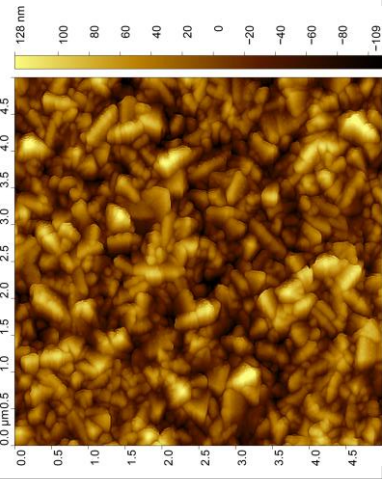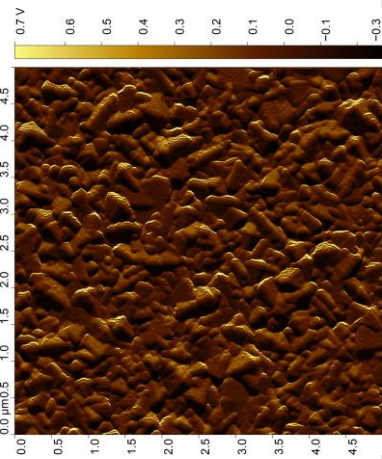
Conditions	FESEM image	AFM image		RMS roughness (nm)
		Height	Phase	
FTO				47.2
Sputtering 150 min				42.7

Table 3 The FESEM and AFM images of TiO$_2$ on FTO. (continued)
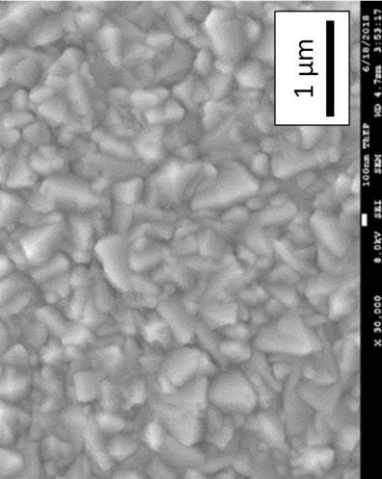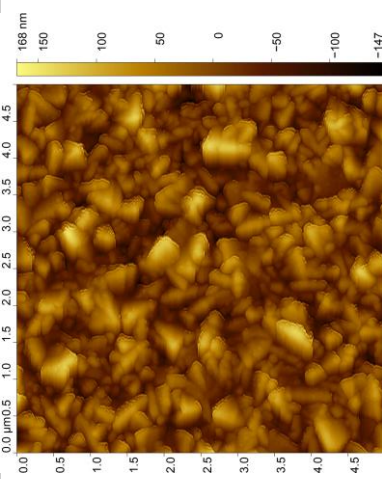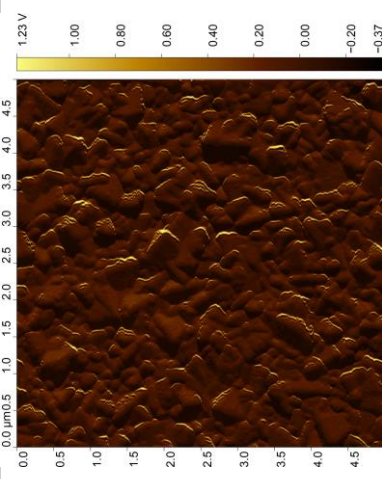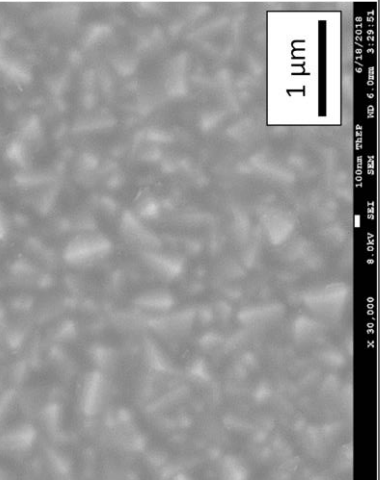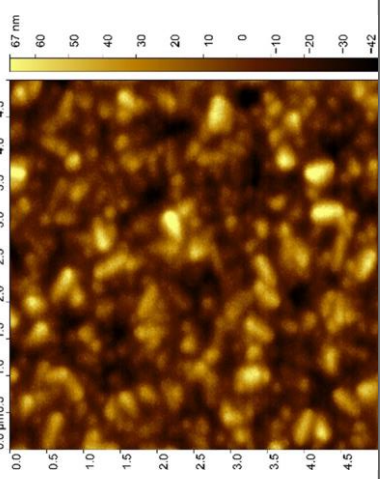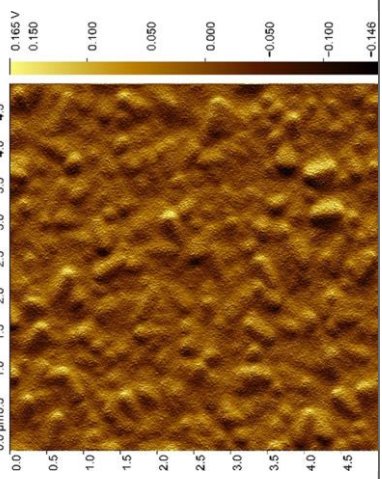
Conditions	FESEM image	AFM image		RMS roughness (nm)
		Height	Phase	
Sputtering 210 min				43.6
Spin coating 2000rpm				19

Table 3 The FESEM and AFM images of TiO$_2$ on FTO. (continued)
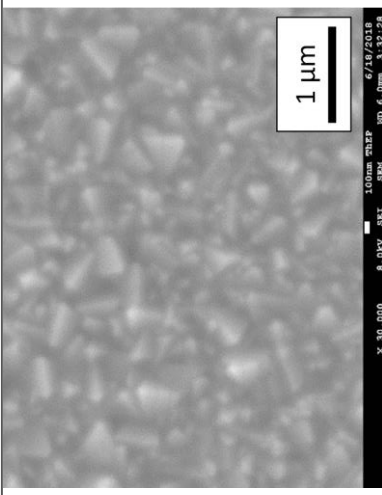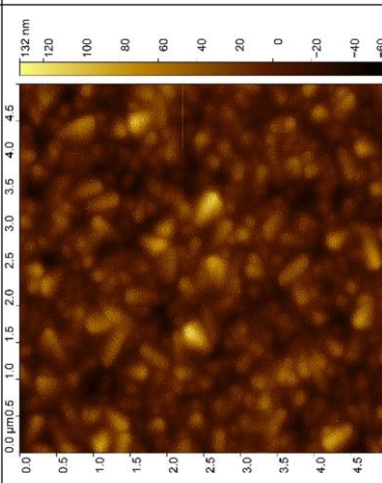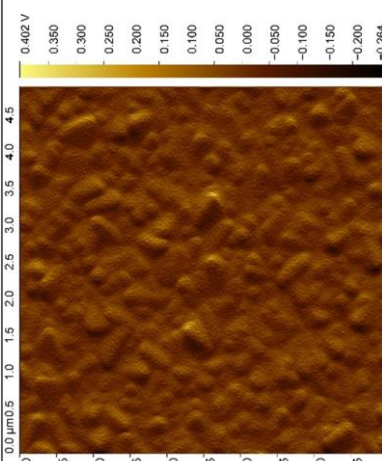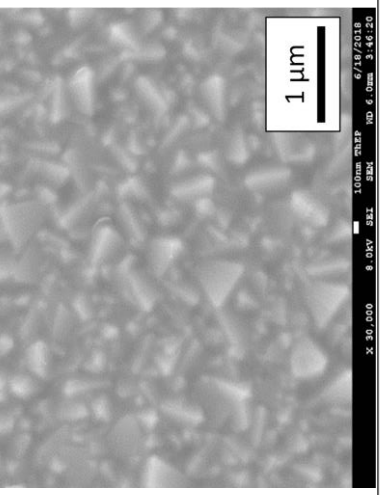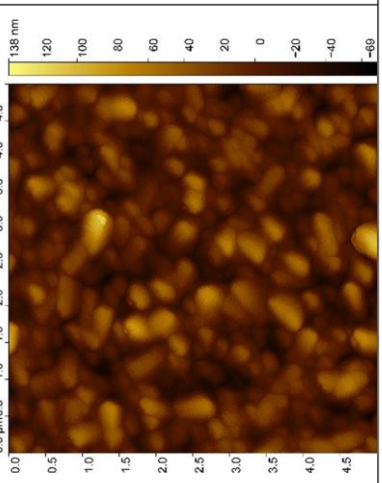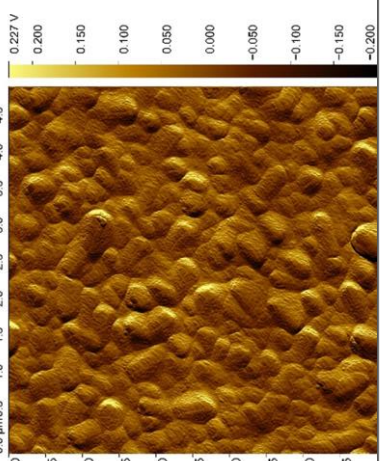
Conditions	FESEM image	AFM image			RMS roughness (nm)
		Height	Phase		
Spin coating 3000rpm					20.5
Spin coating 4000rpm					23.7

Table 3 The FESEM and AFM images of TiO$_2$ on FTO. (continued)
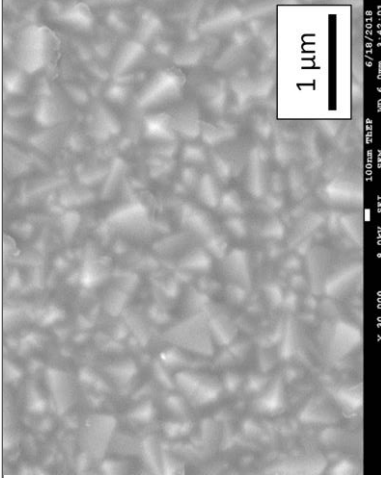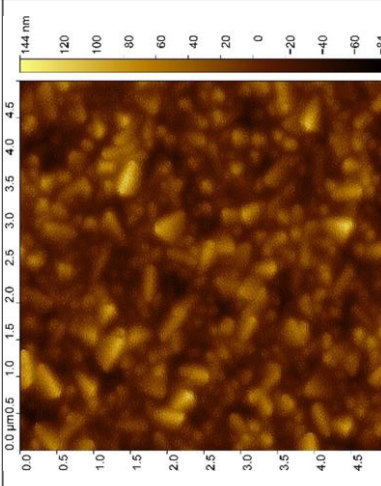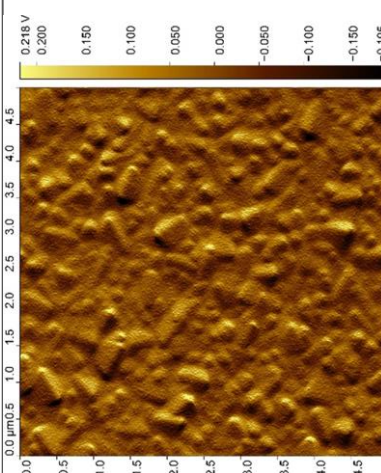
Conditions	FESEM image	AFM image		RMS roughness (nm)
		Height	Phase	
Spin coating 5000rpm				23.3

Table 4 The AFM images of TiO$_2$ on SLG.
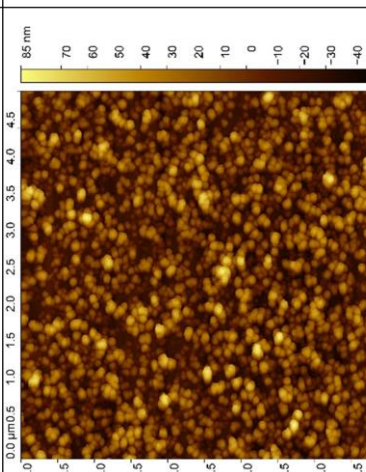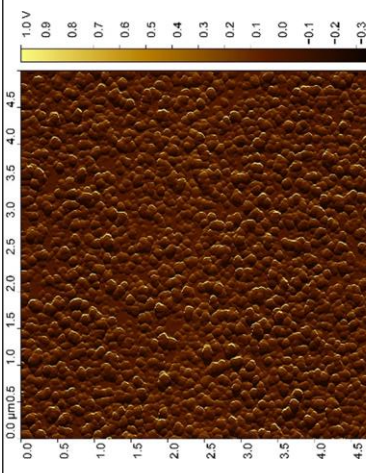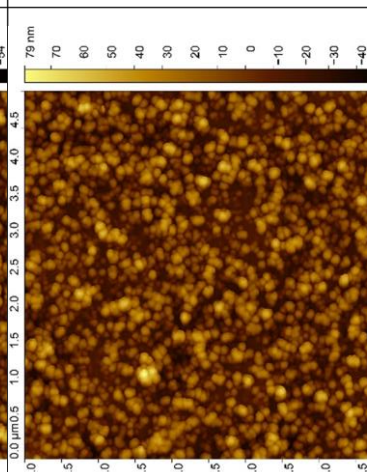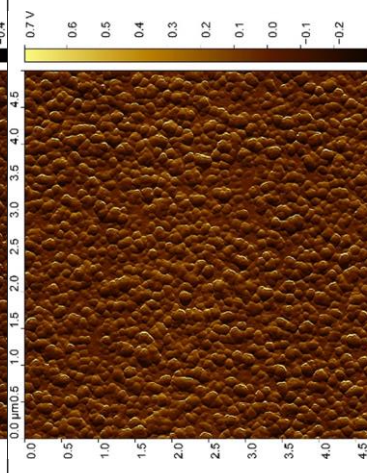
Conditions	AFM image		RMS roughness (nm)
	Height	Phase	
Sputtering 150 min			23.3
Sputtering 210 min			18.8

Table 4 The AFM images of TiO$_2$ on SLG. (continued)

Conditions	AFM image		RMS roughness (nm)
	Height	Phase	
Spin coating 2000rpm			7.18
Spin coating 3000rpm			5.35

Table 4 The AFM images of TiO$_2$ on SLG. (continued)

Conditions	AFM image		RMS roughness (nm)
	Height	Phase	
Spin coating 4000rpm			5.29
Spin coating 5000rpm			2.89

CHAPTER V
RESULTS AND DISCUSSION OF PEROVSKITE SOLAR CELLS

In this chapter, the results of PSCs and the study of the effects of cp-TiO$_2$ layer on the efficiency of the perovskite solar cells are described.

5.1 The morphology of mp-TiO$_2$ layer

The FESEM image (Figure 32(a)) shows that the mp-TiO$_2$ films are homogeneous but porous, and expected to help enhancing electron transport in this scaffold structure due to the increase of the surface area. Figure 32(b) shows that the thickness of mp-TiO$_2$ layer is about 375 nm.

5.2 The morphology of perovskite layer

Figure 33 shows the surface of porous PbI$_2$ film covered on TiO$_2$ scaffold layers. The porous PbI$_2$ films are composed of PbI$_2$ nano-flakes connected to each other. A uniform coverage of PbI$_2$ on the surface could be obtained from spinning PbI$_2$ solution at 3000 rpm for 30 s.
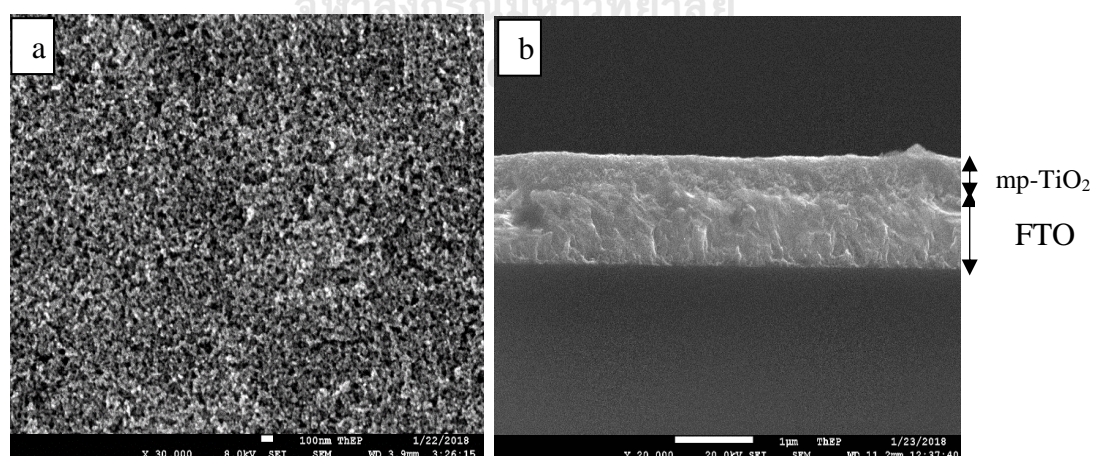
Figure 32 FESEM images of (a) surface morphology and (b) cross-section of mp-TiO$_2$ layer.
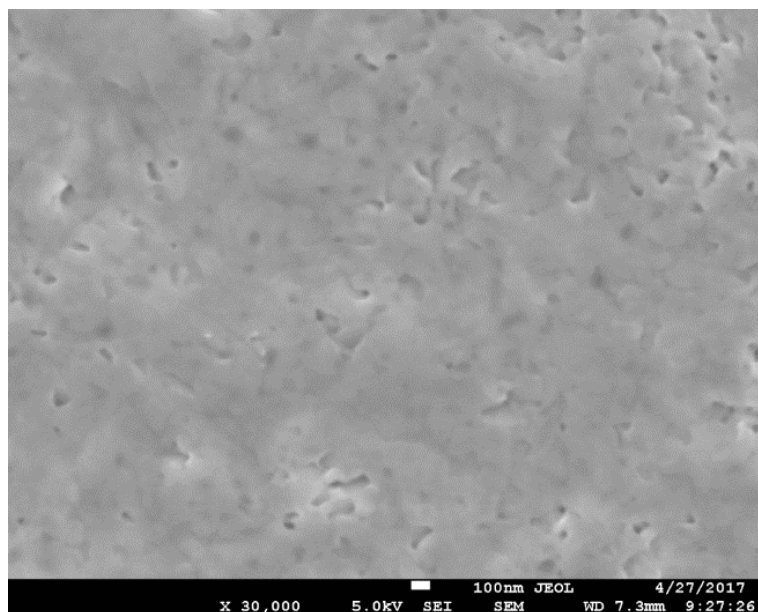
Figure 33 FESEM images of PbI$_2$ layer.
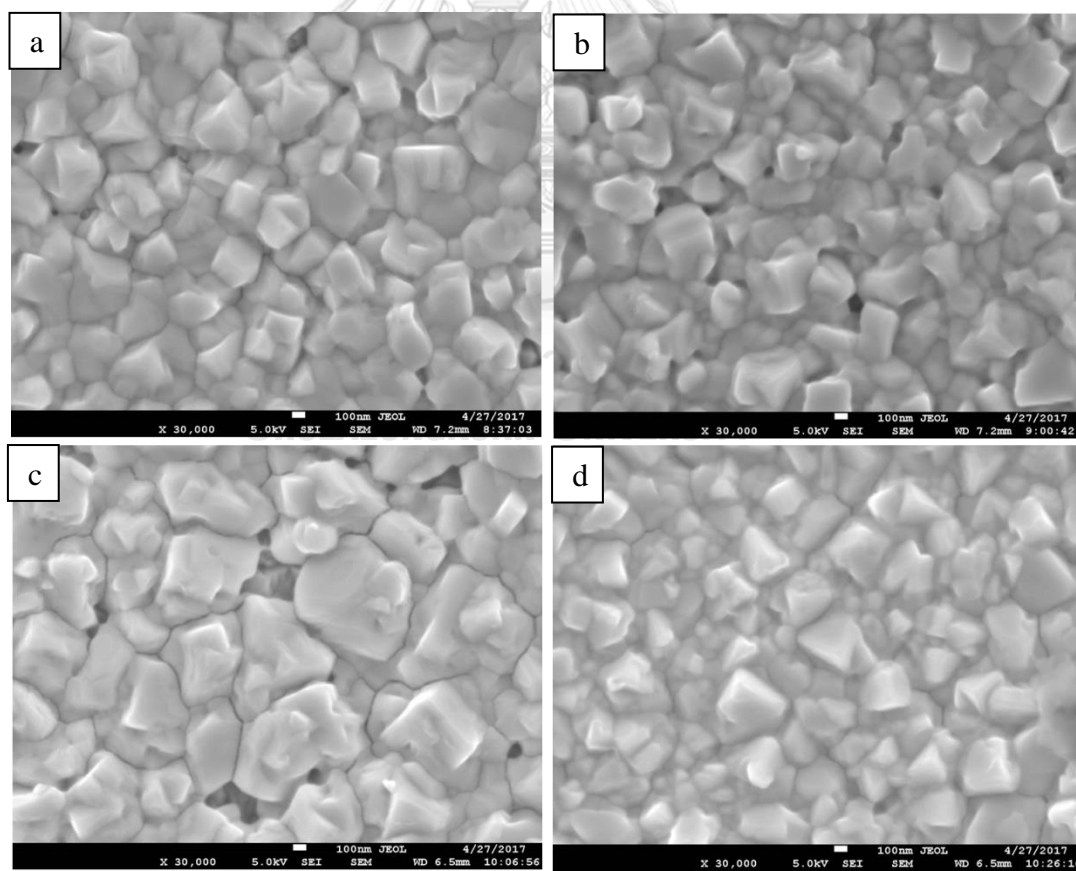
Figure 34 FESEM images of perovskite layers with varying loading time (a) 30 s, (b) 60 s, (c) 120 s, and (d) 600 s.

- CH$_3$NH$_3$PbI$_3$ perovskite layer

Figure 34 shows the FESEM images of perovskite layer with a loading time of 30 s, 60 s, 120 s, and 600 s. The effect of the loading time on morphology of perovskite layers show that 30 s loading time is sufficient because there is a full coverage with uniform grain size compared with others. Therefore, 30 s for loading time of MAI solution was employed in this work. Figure 35 shows the transmittance of PbI$_2$ layer and perovskite layer after spinning MAI on PbI$_2$ layers. With the use of the two-step spin coating method to fabricate the perovskite layer and in order to make sure that most of PbI$_2$ layer has become perovskite layer, the number of times in spinning MAI on PbI$_2$ layers are increased. From this graph, comparing between PbI$_2$ layer and 1, 2 and 3 spinning times of MAI, it is found that the PbI$_2$ layer turns into perovskite material that can absorb light in the range of 750 – 800 nm. Moreover, no difference between 2 and 3 spinning times of MAI can be observed. Thus, in this study, 2 times spinning of MAI were adequate to fabricate the perovskite absorber layer.

In this study, PSC using Au/spiro-OMeTAD/Perovskite/mp-TiO$_2$/cp-TiO$_2$/FTO structure, as shown in Figure 36, was employed. The complete PSCs with cp-TiO$_2$ from (a) the sputtering and (b) the spin coating methods are depicted in Figure 37.
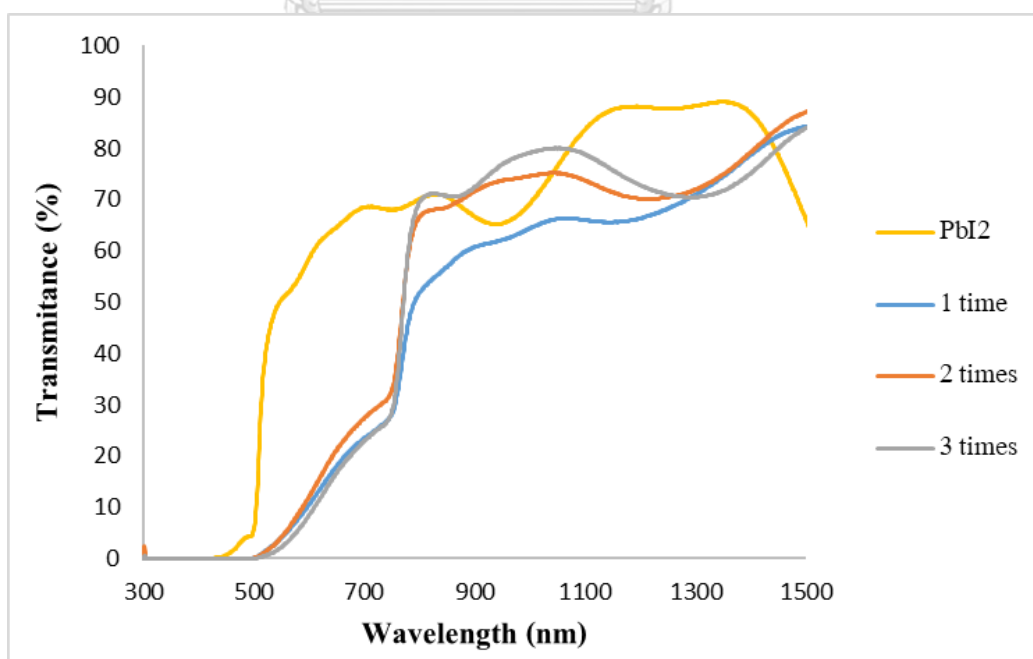
Figure 35 A plot of transmittance of PbI$_2$ layer and times of spinning MAI on PbI$_2$ layers.
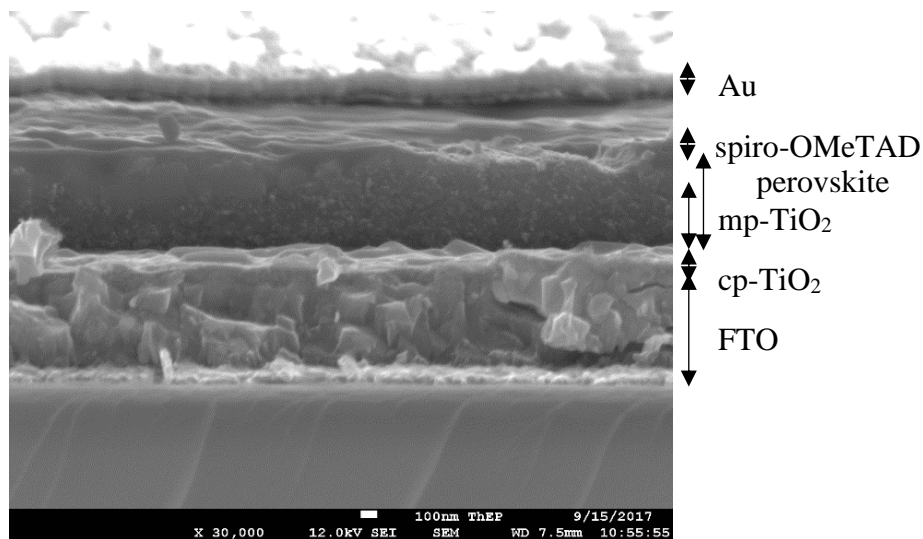
Figure 36 FE-SEM images of cross-section of PSCs.

5.3 Photovoltaic parameters of PSCs

In this work, it was found that the PSC devices with cp-TiO$_2$ layer deposited by the sputtering method showed very small response to light. It is likely that when we sputtered TiO$_2$ from Ti metallic target, it may yield many phases or incomplete structure in the form of TiO$_x$ instead of a preferred anatase phase. The photovoltaic parameters of PSCs with the sputtered cp-TiO$_2$ layer are shown in Table 5.

Figure 38 shows the J-V curves of the PSCs with the spin-coated and sputtered TiO$_2$. Current density of the PSC with sputtered TiO$_2$ layer is less than 4 mA/cm^2 compared to that of PSC from spin-coated TiO$_2$ layer which is up to 16 mA/cm^2. This implies that TiO$_2$ layer from the sputtering method cannot transfer electrons into FTO layer as good as anticipated.

Figure 37 Photographs of complete PSCs with TiO$_2$ from (a) sputtering and (b) spin-coating methods.
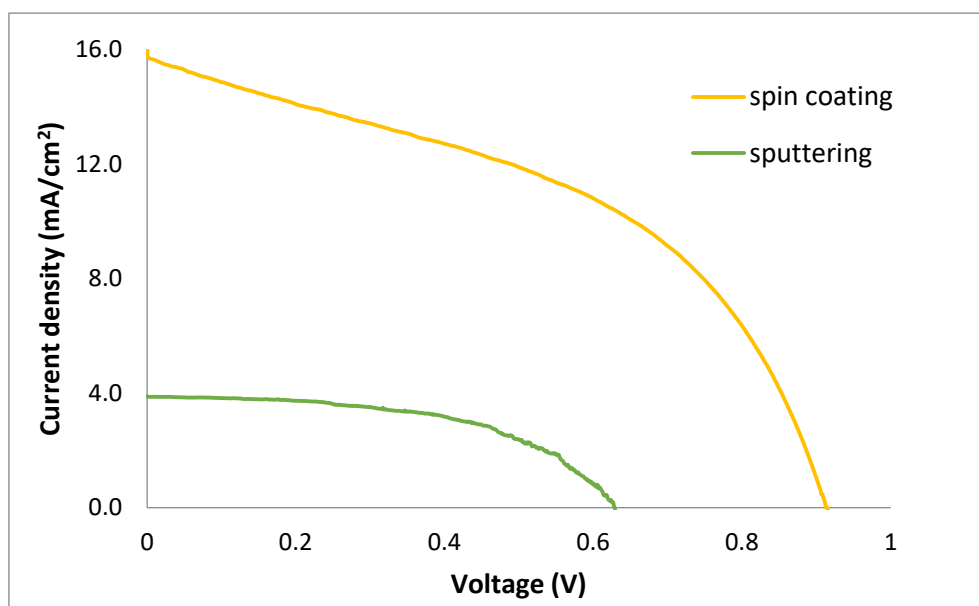
Figure 38 A plot of J-V curves of PSCs with spin-coated and sputtered TiO_2.

Table 5 The photovoltaic parameters of $FTO/cp\text{-}TiO_2/mp\text{-}TiO_2/MAPbI_3/Spiro\text{-}OMeTAD/Au$ with varying deposition time of $cp\text{-}TiO_2$ sputtering (measured on an active area of 0.18 cm^2).

Deposition time (min)	J_{sc} (mA/cm^2)	V_{oc} (V)	FF (%)	PCE (%)	R_{series} (Ω/cm^2)	R_{shunt} (Ω/cm^2)
120	3.882	0.628	53.55	1.31	7.77	2034
150	4.106	0.473	43.83	0.85	9.28	770.4
180	4.544	0.143	51.5	0.33	3.80	51.2
210	3.232	0.451	33.75	0.49	13.76	63.5
240	3.923	0.284	42.41	0.47	9.01	179.4

The photovoltaic parameters of the PSCs with the spin-coated $cp\text{-}TiO_2$ layer are shown in Table 6. The results show that both compact and mesoporous TiO_2 layers are necessary to achieve perovskite solar cell, with PCE higher than 4.5%. However, with only compact or mesoporous TiO_2 layers, our devices yield very low PCE (<1.8%).

For the PSCs with $cp\text{-}TiO_2$ and $mp\text{-}TiO_2$ layers, the average efficiency is about 5.5% and the maximum is 6.55% when the $cp\text{-}TiO_2$ and $mp\text{-}TiO_2$ were spun at 5000 rpm for 30 s. The open-circuit voltage and the short-circuit current density of the best

device is 915 mV and 16.02 mA/cm^2, respectively. However, the fill factor is only 44.70%, i.e. the junction formation is not quite good. Moreover, all of the layers in the PSCs were fabricated by spin coating method that can cause the variation in the uniformity of the films resulting in undesirably high series resistance and low shunt resistance.

Table 6 The photovoltaic parameters of the perovskite solar cells with varying cp-TiO$_2$ and mp-TiO$_2$ (measured on an active area of 0.18 cm^2).

Spin speed/time		J_{sc}	V_{oc}	FF	PCE	R_{series}	R_{shunt}
cp-TiO$_2$	mp-TiO$_2$	(mA/cm^2)	(V)	(%)	(%)	(Ω/cm^2)	(Ω/cm^2)
3000rpm/30s	5000rpm/30s	14.78	0.883	46.13	6.02	8.13	205.9
		13.68	0.920	43.71	5.50	9.62	297.8
		12.46	0.913	45.01	5.12	9.10	244.6
4000rpm/30s	5000rpm/30s	13.62	0.912	46.70	5.80	8.63	94.2
		9.39	0.954	53.00	4.75	11.10	62.3
		10.75	0.910	46.17	4.52	9.72	205.4
5000rpm/30s	5000rpm/30s	16.02	0.915	44.70	6.55	8.24	122.1
		13.27	0.884	54.50	6.39	6.29	103.1
		9.39	0.950	57.08	5.09	9.08	66.2
3000rpm/30s	-	7.27	0.840	24.41	1.49	88.36	99.7
4000rpm/30s	-	8.14	0.160	22.91	0.31	9.35	20.9
5000rpm/30s	-	10.04	0.640	27.42	1.78	34.38	85.8
-	5000rpm/30s	4.89	0.690	30.61	1.04	33.65	75.2

CHAPTER VI
SUMMARY

This research presents the properties of TiO_2 layer fabricated by sputtering and spin coating methods and their effects on the performance and the photovoltaic parameters of the $MAPbI_3$ perovskite solar cells.

The reactive RF magnetron sputtering was used to fabricate transparent TiO_2 ultra-thin film from a Ti metallic target. The suitable sputtering conditions were 200 W of RF power, sputtering pressure of 1.1×10^{-3} mbar with 50% of $O_2/(O_2+Ar)$ ratio for the sputtering time of 180 minutes or more. This gave a thickness of TiO_2 compact layer of approximately 25 nm. It can selectively block the transport of holes from TiO_2 to the FTO layer as indicated by the diode behavior in the I-V characteristics between the TiO_2/FTO interface and should be able to be used as electron transport material in perovskite solar cells. However, the cp-TiO_2 fabricated by sputtering method did not give a positive result when integrated in our perovskite solar cells, i.e. the TiO_2 layers fabricated from Ti metallic sputtering target might not be suitable for transferring of electrons from the perovskite layer to the FTO. The existence of the TiO_2 layer fabricated by sputtering method could not easily be identified due to its ultra-thin thickness. It did not change the surface morphology of the underlying FTO surface as investigated by FESEM. On the other hand, the AFM images show the alterations on the surface of TiO_2/FTO in such a way that the sharpness of the grains reduces significantly and the rms roughness of the surface of TiO_2/FTO decreases from ~50 nm (bare FTO) to ~20 nm as well as the reduction in the z-range of the TiO_2/FTO surface. In addition, very fine round grains in the phase images of spin-coated TiO_2 on the larger FTO grains were observed, and consistent with the shape of TiO_2 grains seen on the SLG substrates. This indicates the existence of the spin-coated cp-TiO_2 layer on the FTO surface which is not visible on the sputter-coated TiO_2/FTO by either FESEM or AFM.

Besides, there are also other factors of the sputtering process that affect the properties of the film such as target size, power, power density, target – substrate distance, and sputter gas pressure. These factors depend on sputtering equipment used to fabricate TiO_2. In this work, TiO_2 fabricated by sputtering could not be used in the

PSCs due to the conditions in the process. Table 7 shows comparison of sputtering conditions of TiO_2 between this work and the other work [24] that has been used to produce solar cells from TiO_2.

Since the maximum power of our system is only 300 W and our target size is much larger, as a result, the power density in our system is lower than that of the other work. Moreover, the volume of our chamber is large and the pressure of O_2 gas cannot exceed 0.750 mTorr which can cause the pumping system to stop working. Therefore, it is not possible to use sputtering gas pressure and $O_2/(O_2+Ar)$ ratio as in the other work.

Despite the fact that the spin-coated TiO_2 layer cannot completely block the transport of holes from TiO_2 to the FTO layer and do not have a uniform film as that from the sputtering technique, it can be used to fabricate the PSCs. However, the I-V curves show some current leakage in the reverse bias. The morphology of the spin-coated cp-TiO_2 shows very fine and round grains on the underlying FTO surface. This results in the increase of the surface area leading to the increase of photo-generated currents in the PSCs.

It is worth noting that the XRD cannot be used to confirm the existence of a very thin layer of the cp-TiO_2 on the FTO substrate because the thickness of the cp-TiO_2 is only a few unit cells. As a result, the intensities of diffraction peaks could not be detected.

Table 7 Sputtering conditions of TiO_2.

	This work	**Other work [24]**
target	Ti	Ti
RF power	200 W	130 W
target area	81.07 cm^2	2 cm^2
power density	2.47 W/cm^2	65 W/cm^2
sputter gas pressure	0.82 mTorr	10 mTorr
$O_2/(O_2+Ar)$	30%, 50%	20%

Lastly, the PSCs in this work required both the cp-TiO$_2$ and the mp-TiO$_2$ layers in order to produce working devices. The best condition was achieved by spinning both cp-TiO$_2$ and mp-TiO$_2$ at 5,000 rpm for 30 s. It was found that the maximum power conversion efficiency is 6.55%. However, the junction formation of PSCs are not good as indicated by the fill factor of 44.7% which is lower than a typical requirement of 70%. There are still many factors affecting the low value of fill factor such as the non-uniformity, non-homogeneity of the coating layers that is consistent with low shunt resistance and high series resistance of the devices obtained in this work.

For the future work, the morphology of cp-TiO$_2$ fabricated by spin coating method may be improved for higher PCE of the PSCs by optimizing the other factors such as changing concentration of TiO$_2$ solution, annealing temperature, and humidity, etc. Moreover, there are many other factors required to achieve high PCE of the PSCs. The morphology and grain size of perovskite are the factors among others because uniform perovskite films with high surface coverage can also affect the transport of electrons and holes.

REFERENCES

1. Lizin, S., et al., *The future of organic photovoltaic solar cells as a direct power source for consumer electronics.* Solar Energy Materials and Solar Cells, 2012. **103**: p. 1-10.

2. Grätzel, M., *Recent Advances in Sensitized Mesoscopic Solar Cells.* Accounts of Chemical Research, 2009. **42**(11): p. 1788-1798.

3. Pan, Z., et al., *High-Efficiency "Green" Quantum Dot Solar Cells.* Journal of the American Chemical Society, 2014. **136**(25): p. 9203-9210.

4. Wang, J., et al., *Core/Shell Colloidal Quantum Dot Exciplex States for the Development of Highly Efficient Quantum-Dot-Sensitized Solar Cells.* Journal of the American Chemical Society, 2013. **135**(42): p. 15913-15922.

5. Kamat, P.V., *Organometal Halide Perovskites for Transformative Photovoltaics.* Journal of the American Chemical Society, 2014. **136**(10): p. 3713-3714.

6. Green, M.A., A. Ho-Baillie, and H.J. Snaith, *The emergence of perovskite solar cells.* Nat Photon, 2014. **8**(7): p. 506-514.

7. Borriello, I., G. Cantele, and D. Ninno, *Ab initio.* Physical Review B, 2008. **77**(23): p. 235214.

8. O'Regan, B. and M. Grätzel, *A low-cost, high-efficiency solar cell based on dye-sensitized colloidal TiO2 films.* Nature, 1991. **353**: p. 737.

9. Yella, A., et al., *Porphyrin-Sensitized Solar Cells with Cobalt (II/III)–Based Redox Electrolyte Exceed 12 Percent Efficiency.* Science, 2011. **334**(6056): p. 629.

10. Bach, U., et al., *Solid-state dye-sensitized mesoporous TiO2 solar cells with high photon-to-electron conversion efficiencies.* Nature, 1998. **395**(6702): p. 583-585.

11. Kim, H.-S., et al., *Lead Iodide Perovskite Sensitized All-Solid-State Submicron Thin Film Mesoscopic Solar Cell with Efficiency Exceeding 9%.* Scientific Reports, 2012. **2**: p. 591.

12. Lee, M.M., et al., *Efficient Hybrid Solar Cells Based on Meso-Superstructured Organometal Halide Perovskites.* Science, 2012. **338**(6107): p. 643.

13. Etgar, L., et al., *Mesoscopic CH3NH3PbI3/TiO2 Heterojunction Solar Cells.* Journal of the American Chemical Society, 2012. **134**(42): p. 17396-17399.

14. Cameron, P.J. and L.M. Peter, *Characterization of Titanium Dioxide Blocking Layers in Dye-Sensitized Nanocrystalline Solar Cells.* The Journal of Physical Chemistry B, 2003. **107**(51): p. 14394-14400.

15. Kavan, L., et al., *Electrochemical Characterization of TiO2 Blocking Layers for Dye-Sensitized Solar Cells.* The Journal of Physical Chemistry C, 2014. **118**(30): p. 16408-16418.

16. Unger, E.L., et al., *Effect of the Preparation Procedure on the Morphology of Thin TiO2 Films and Their Device Performance in Small-Molecule Bilayer Hybrid Solar Cells.* ACS Applied Materials & Interfaces, 2012. **4**(11): p. 5997-6004.

17. Xia, J., et al., *Deposition of a Thin Film of TiOx from a Titanium Metal Target as Novel Blocking Layers at Conducting Glass/TiO2 Interfaces in Ionic Liquid*

Mesoscopic TiO2 Dye-Sensitized Solar Cells. The Journal of Physical Chemistry B, 2006. **110**(50): p. 25222-25228.

18. Ke, W., et al., *An efficient and transparent copper sulfide nanosheet film counter electrode for bifacial quantum dot-sensitized solar cells.* Journal of Power Sources, 2014. **248**: p. 809-815.

19. Chandiran, A.K., et al., *Low-Temperature Crystalline Titanium Dioxide by Atomic Layer Deposition for Dye-Sensitized Solar Cells.* ACS Applied Materials & Interfaces, 2013. **5**(8): p. 3487-3493.

20. Kavan, L., et al., *Preparation of TiO2 (anatase) films on electrodes by anodic oxidative hydrolysis of TiCl3.* Journal of Electroanalytical Chemistry, 1993. **346**(1): p. 291-307.

21. Gao, Q., et al., *An Effective TiO2 Blocking Layer for Perovskite Solar Cells with Enhanced Performance.* Chemistry Letters, 2015. **44**(5): p. 624-626.

22. Chen, C., et al., *Radio Frequency Magnetron Sputtering Deposition of TiO2 Thin Films and Their Perovskite Solar Cell Applications.* Scientific Reports, 2015. **5**: p. 17684.

23. Yang, D., et al., *Alternating precursor layer deposition for highly stable perovskite films towards efficient solar cells using vacuum deposition.* Journal of Materials Chemistry A, 2015. **3**(18): p. 9401-9405.

24. S Mali, S. and C. Hong, *Efficient planar n-i-p type heterojunction flexible perovskite solar cells with sputtered TiO2 electron transporting layers*. Vol. 9. 2017.

25. Song, J., et al., *Low-temperature SnO2-based electron selective contact for efficient and stable perovskite solar cells.* Journal of Materials Chemistry A, 2015. **3**(20): p. 10837-10844.

26. Gubbala, S., et al., *Band-Edge Engineered Hybrid Structures for Dye-Sensitized Solar Cells Based on SnO2 Nanowires.* Advanced Functional Materials, 2008. **18**(16): p. 2411-2418.

27. Lee, W.S., Y.-S. Park, and Y.-K. Cho, *Hierarchically Structured Suspended TiO2 Nanofibers for Use in UV and pH Sensor Devices.* ACS Applied Materials & Interfaces, 2014. **6**(15): p. 12189-12195.

28. Roy, P., et al., *TiO2 nanotubes and their application in dye-sensitized solar cells.* Nanoscale, 2010. **2**(1): p. 45-59.

29. Nunes, D., et al., *Photocatalytic behavior of TiO2 films synthesized by microwave irradiation.* Catalysis Today, 2016. **278**: p. 262-270.

30. Chae, S.Y., et al., *Preparation of Size-Controlled TiO2 Nanoparticles and Derivation of Optically Transparent Photocatalytic Films.* Chemistry of Materials, 2003. **15**(17): p. 3326-3331.

31. Golobostanfard, M.R. and H. Abdizadeh, *Effect of mixed solvent on structural, morphological, and optoelectrical properties of spin-coated TiO2 thin films.* Ceramics International, 2012. **38**(7): p. 5843-5851.

32. Di Paola, A., M. Bellardita, and L. Palmisano, *Brookite, the Least Known TiO2 Photocatalyst.* Catalysts, 2013. **3**(1).

33. Lin, H., et al., *Size dependency of nanocrystalline TiO2 on its optical property and photocatalytic reactivity exemplified by 2-chlorophenol.* Applied Catalysis B: Environmental, 2006. **68**(1–2): p. 1-11.

34. Nunes, D., et al., *{Photocatalytic behavior of TiO2 films synthesized by microwave irradiation}.* Catalysis Today, 2015.

35. Fujishima, A., T.N. Rao, and D.A. Tryk, *Titanium dioxide photocatalysis.* Journal of Photochemistry and Photobiology C: Photochemistry Reviews, 2000. **1**(1): p. 1-21.

36. Sun, W., et al., *Controllable synthesis and morphology-dependent photocatalytic performance of anatase TiO2 nanoplates.* RSC Advances, 2015. **5**(1): p. 513-520.

37. Pimentel, A., et al., *Photocatalytic Activity of TiO2 Nanostructured Arrays Prepared by Microwave-Assisted Solvothermal Method*, in *Semiconductor Photocatalysis - Materials, Mechanisms and Applications*, W. Cao, Editor. 2016, InTech: Rijeka. p. Ch. 03.

38. De Wolf, S., et al., *Organometallic Halide Perovskites: Sharp Optical Absorption Edge and Its Relation to Photovoltaic Performance.* The Journal of Physical Chemistry Letters, 2014. **5**(6): p. 1035-1039.

39. Kim, H.-S., et al., *High Efficiency Solid-State Sensitized Solar Cell-Based on Submicrometer Rutile TiO2 Nanorod and CH3NH3PbI3 Perovskite Sensitizer.* Nano Letters, 2013. **13**(6): p. 2412-2417.

40. Stranks, S.D., et al., *Electron-Hole Diffusion Lengths Exceeding 1 Micrometer in an Organometal Trihalide Perovskite Absorber.* Science, 2013. **342**(6156): p. 341.

41. Fan, J., B. Jia, and M. Gu, *Perovskite-based low-cost and high-efficiency hybrid halide solar cells.* Photonics Research, 2014. **2**(5): p. 111-120.

42. K. Maurya, D., A. Sardarinejad, and K. Alameh, *Recent Developments in R.F. Magnetron Sputtered Thin Films for pH Sensing Applications—An Overview.* 2014.

43. *<Spin Coating Info.pdf>.*

44. Shi, S., et al., *Advancements in all-solid-state hybrid solar cells based on organometal halide perovskites.* Materials Horizons, 2015. **2**(4): p. 378-405.

45. Moore, D.T., et al., *Impact of the organic halide salt on final perovskite composition for photovoltaic applications.* APL Materials, 2014. **2**(8): p. 081802.

46. Cohen, B.-E., S. Gamliel, and L. Etgar, *Parameters influencing the deposition of methylammonium lead halide iodide in hole conductor free perovskite-based solar cells.* APL Materials, 2014. **2**(8): p. 081502.

47. Im, J.-H., et al., *Growth of CH3NH3PbI3 cuboids with controlled size for high-efficiency perovskite solar cells.* Nat Nano, 2014. **9**(11): p. 927-932.

48. Liu, M., M.B. Johnston, and H.J. Snaith, *Efficient planar heterojunction perovskite solar cells by vapour deposition.* Nature, 2013. **501**(7467): p. 395-398.

49. Hu, H., et al., *Vapour-based processing of hole-conductor-free CH3NH3PbI3 perovskite/C60 fullerene planar solar cells.* RSC Advances, 2014. **4**(55): p. 28964-28967.

50. Chen, Q., et al., *Planar Heterojunction Perovskite Solar Cells via Vapor-Assisted Solution Process.* Journal of the American Chemical Society, 2014. **136**(2): p. 622-625.

51. Pankove, J.I., *Optical Processes in Semiconductors.* 2012: Dover Publications.

52. Shi, Y., et al., *The structure and function of cell membranes studied by atomic force microscopy.* Seminars in Cell & Developmental Biology, 2018. **73**: p. 31-44.
53. E Dann, S., *Reactions and Characterization of Solids*. 2000, Loughborough University.
54. Panda, B., *STRUCTURAL AND ELECTRONIC PROPERTIES OF CHALCOPYRITE SEMICONDUCTORS*, in *Department Of Physics*. 2011: National Institute Of Technology, Rourkela.
55. Ogawa, H., et al., *Growth of TiO2 thin film by reactive RF magnetron sputtering using oxygen radical.* Journal of Alloys and Compounds, 2008. **449**(1): p. 375-378.
56. Senthil Kumar, V., *Effects of Annealing treatment on optical properties of anatase TiO2 thin films*. Vol. 3. 2011. 42-48.

จุฬาลงกรณ์มหาวิทยาลัย
CHULALONGKORN UNIVERSITY

APPENDIX

VITA

Ramon Songtanasit was born on 16th March 1992 in Bangkok, Thailand. She received the Bachelor degree of Science on Physics from department of Physics, faculty of Science,Chulalongkorn University in 2014.